nature neuroscience

ARTICLES

https://doi.org/10.1038/s41593-020-00776-3

Check for updates

Targeted photostimulation uncovers circuit motifs supporting short-term memory

Kayvon Daie[1], Karel Svoboda[1]✉ and Shaul Druckmann[1,2]✉

Short-term memory is associated with persistent neural activity that is maintained by positive feedback between neurons. To explore the neural circuit motifs that produce memory-related persistent activity, we measured coupling between functionally characterized motor cortex neurons in mice performing a memory-guided response task. Targeted two-photon photostimulation of small (<10) groups of neurons produced sparse calcium responses in coupled neurons over approximately 100 µm. Neurons with similar task-related selectivity were preferentially coupled. Photostimulation of different groups of neurons modulated activity in different subpopulations of coupled neurons. Responses of stimulated and coupled neurons persisted for seconds, far outlasting the duration of the photostimuli. Photostimuli produced behavioral biases that were predictable based on the selectivity of the perturbed neuronal population, even though photostimulation preceded the behavioral response by seconds. Our results suggest that memory-related neural circuits contain intercalated, recurrently connected modules, which can independently maintain selective persistent activity.

Short-term memory circuits produce persistent activity in response to brief inputs[1–3]. As individual neurons respond transiently to short stimuli, persistent activity probably requires positive feedback between neurons[4,5]. A variety of network models, distinguished by different circuit motifs, can maintain persistent activity[4,6–9]. Brain regions with memory-related activity generally show strong correlations in neural activity, both across neurons and over time, often referred to as low-dimensional circuit dynamics[10,11]. Many different networks can create these correlated dynamics. Recordings of neural activity alone are therefore insufficient to infer which, if any, model network is implemented in the brain[12,13].

In mice performing a memory-guided, directional licking task, anterolateral motor cortex (ALM) neurons exhibit low-dimensional[14,15] persistent activity that predicts the direction of upcoming movements[3]. Such persistent activity is often modeled as a low-dimensional attractor circuit[8], in which all neurons with similar task-related selectivity are strongly coupled to each other. Attractor circuits are thus expected to respond to brief perturbations of arbitrary groups of neurons with a consistent pattern of low-dimensional activity that preserves the network's overall correlation structure[5]. In contrast, connectivity in cortical networks tends to be sparse and local[16–18], suggestive of interdigitated subnetworks with strong connectivity within a subnetwork and weak connections between subnetworks[19,20]. The consequences of these circuit motifs for dynamics in short-term memory circuits are unclear.

We used targeted photostimulation and calcium imaging to probe functional circuit motifs in ALM during behavior. Targeted photostimulation produced persistent changes in a sparse subset of neurons, indicating a modular, high-dimensional circuit architecture, with preferential connectivity between nearby neurons with similar tuning. The persistent changes in the activity of ALM evoked by photostimulation of a handful of neurons (<10) were sufficiently strong and long lasting to produce biases in behavior several seconds after the photostimulus. Our results imply a modular circuit architecture with variable between-module connections in which each module independently produces persistent activity.

Results

Targeted photostimulation of persistent activity in ALM. Mice expressing the calcium indicator GCaMP6s[21] and the light-activated cation channel soma-targeted (ST) ChrimsonR[17,22] (Extended Data Fig. 1) were trained to discriminate two tones. After a delay epoch lasting 3 s, mice reported the identity of the tone with directional licking (Fig. 1a)[15]. We imaged activity in layer 2/3 (125–250 µm deep; typical field of view (FOV) 600×600 µm^2) of left ALM (8 mice, 84 sessions, 324 trials per session; range, 208–441 trials; Extended Data Fig. 1). On average, 49 neurons (range, 14–98, 75% confidence interval (CI); 25% of the imaged population) per FOV showed significant selectivity during the delay and early response epochs (mean, 26 right and 23 left selective, Extended Data Fig. 2; one-tailed Student's t-test, $P<0.05$)[23,24].

To probe the circuit basis of persistent activity we used two-photon photostimulation of small groups of neurons (Fig. 1b,c) and measured responses in other neurons in the same imaging plane (Fig. 1d–f). We targeted 'photostimulation groups' (pg) consisting of eight neurons each (the photostimulation protocol was designed to alter local network activity by manipulating sparse subsets of selective neurons; Methods). Targeted neurons were photostimulated by scanning the beam over their cell bodies for 3 ms (Extended Data Fig. 3), causing short-latency (mean, 5±2 ms (mean±s.e.m.)) spikes (range, 0.2–1.5 spikes per stimulus) (Extended Data Fig. 3). Neurons in photostimulation groups were photostimulated sequentially, 10 times at 31.25 Hz (total duration, 319 ms; Extended Data Fig. 3). A large proportion (85%, $P<0.05$, one-tailed Student's t-test) of targeted neurons responded with increases in GCaMP6s fluorescence ($\Delta F/F$; mean, 0.43; range, 0.07–0.80, 75% CI). Photostimuli were applied during the delay epoch (on 33.3% or 40% of trials). Multiple (two to five) photostimulation groups were photostimulated during each behavioral session. Neurons were selected for photostimulation based on their trial-type selectivity (Methods). Some groups contained mostly left-selective neurons (Fig. 1d–f, top), whereas others were mainly right selective (Fig. 1d–f, bottom).

[1]Janelia Research Campus, Howard Hughes Medical Institute, Ashburn, VA, USA. [2]Stanford University, Stanford, CA, USA. ✉e-mail: svobodak@janelia.hhmi.org; shauld@stanford.edu

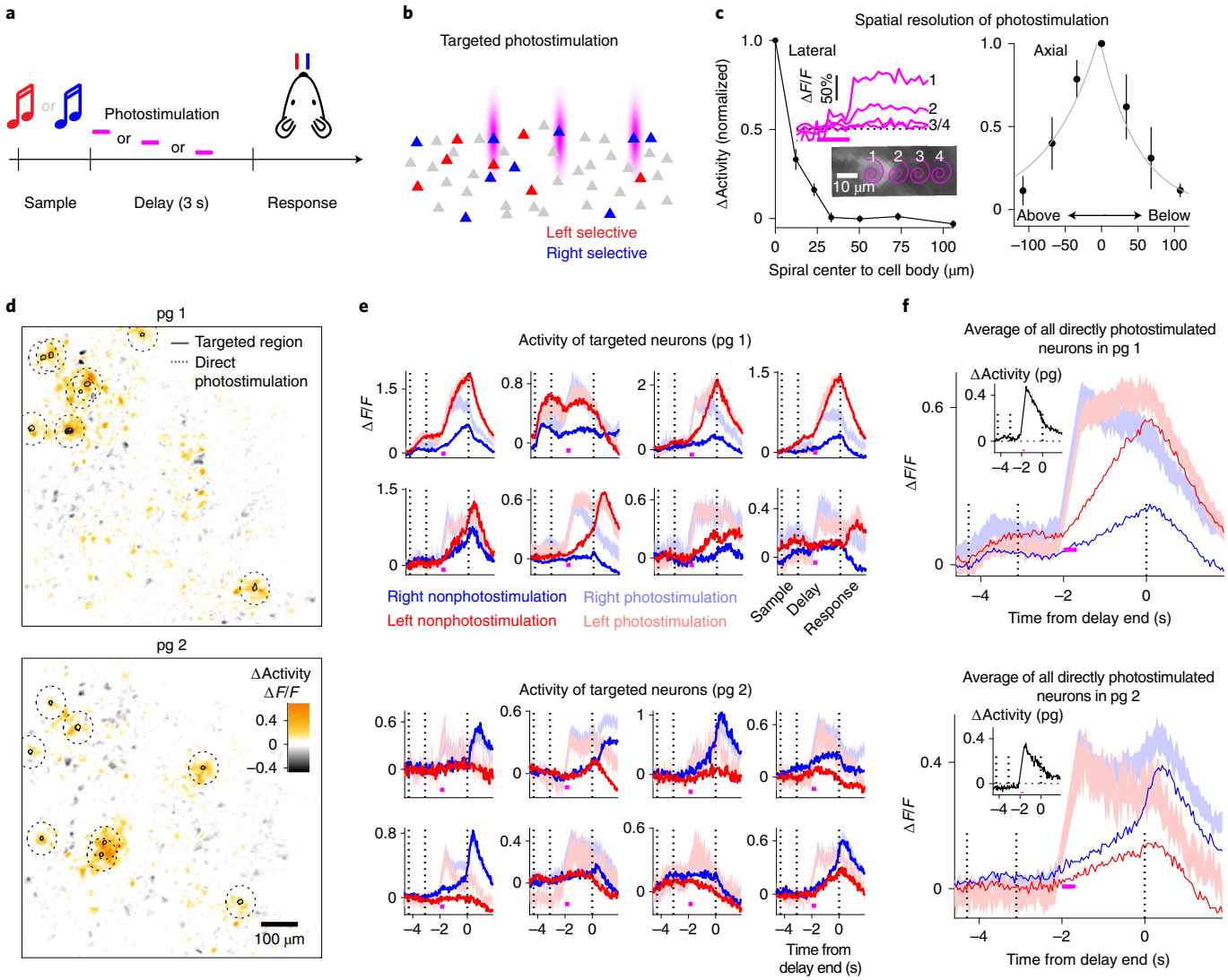

Fig. 1 | Targeted photostimulation during performance of the delayed-response task. a, Task structure. During the sample epoch, mice were instructed by an auditory cue to lick left or lick right for a water reward. Responses were allowed after a 3-s-long delay epoch. Photostimuli (magenta bars) were delivered on a random subset of trials during the delay epoch. **b**, Targeted photostimulation. Two-photon imaging was used to map selectivity of individual neurons during behavior (lick left, red; lick right, blue). Two-photon photostimulation was used to activate groups of neurons based on their selectivity. Magenta shading illustrates spatial resolution of photostimulation (**c**, Extended Data Fig. 4). **c**, Measurement of lateral (left panel) and axial (right panel) spatial resolution of photostimulation. Change in GCaMP6s fluorescence (normalized by response at distance = 0) versus distance between photostimulus (spiral) and imaged neuron (nine neurons). Inset: responses to photostimuli delivered at different lateral distances (0, 12.5, 25 and 37.5 μm, corresponding to labels 1, 2, 3 and 4) (magenta bar, photostimulation, 320 ms). Magenta spirals illustrate an example experiment (error bars, s.e.m.). **d**–**f**, Top: photostimulation group (pg) 1; bottom: photostimulation group 2. **d**, Example photostimulation experiment. Black regions of interest indicate targeted neurons. Dashed circles (radius 20 μm) indicate regions with neurons that could be receiving direct photostimulation. Pixel color indicates the fractional difference in fluorescence between photostimulation and nonphotostimulation trials, averaged over 500 ms after the photostimulus (excited coupled neurons: 22 in group 1, 23 in group 2; inhibited coupled neurons: 6 in group 1, 7 in group 2; $P < 0.05$, one-tailed Student's t-test to determine significance of coupling). **e**, Fluorescence changes (averaged across correct trials) for each of the eight targeted neurons per photostimulation group on photostimulation (light traces) and nonphotostimulation (dark traces) trials (trial types: red, left; blue, right; error shade = s.e.m.). **f**, Responses averaged across all directly photostimulated neurons per photostimulation group. Inset: difference in activity between photostimulation and nonphotostimulation trials, averaged across all directly photostimulated neurons in a photostimulation group (Δactivity pg).

In addition to targeted neurons, cells up to 20 μm laterally from the center of the photostimulus could have been directly photostimulated (Fig. 1c and Extended Data Fig. 4). We refer to activated neurons in this neighborhood together (that is, including the targeted neurons) as 'directly photostimulated' (Fig. 1f). The selectivity of the directly photostimulated population was dominated by the targeted neurons (Extended Data Fig. 4). Neural activity >30 μm from the targeted neurons changed as well (Fig. 1d). Changes in activity >30 μm from a photostimulus result from synaptic interactions with the directly photostimulated population (Fig. 1c and Extended Data Fig. 4). We refer to these neurons as 'coupled'. Photostimulation groups produced detectable excitation (two-tailed Student's t-test, $P < 0.05$) in 20 coupled neurons on average (range, 4–39 neurons, 75% CI; $\Delta F/F$: mean, 0.21, range, 0.07–0.38, 75% CI), and inhibition in 6 coupled neurons on average (range, 0–13 neurons, 75% CI) per FOV. The number of excited coupled neurons decreased with

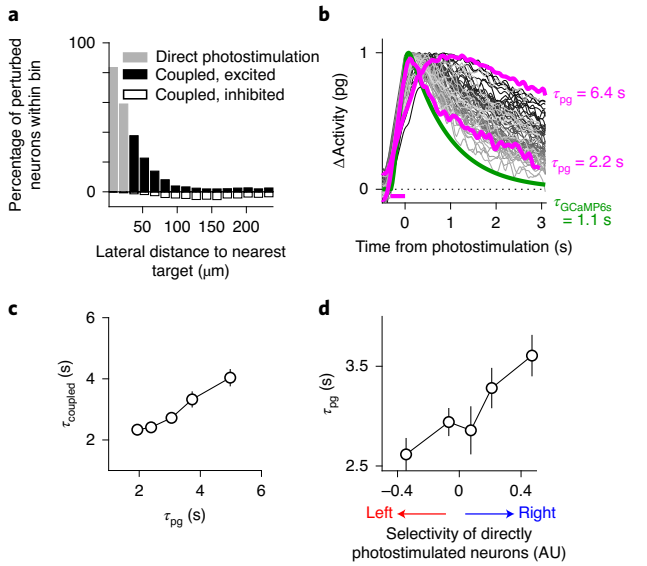

Fig. 2 | Network response to targeted photostimulation. a, Percentage of neurons with activity that is directly excited (gray) or coupled (black, excited; white, inhibited) by photostimulation, as a function of distance (from the nearest photostimulation target). **b**, Decay times (τ_{pg}) of Δactivity pg (Fig. 1f, inset). Traces are color coded based on decay time (gray lines). The green line is fluorescence decay after a brief burst of activity (measurement in Extended Data Fig. 5). The horizontal magenta bar is the time of photostimulation. Magenta traces are two example photostimulation groups with long (6.4-s) and short (2.2-s) time constants. **c**, Decay time constants of coupled neurons ($\tau_{coupled}$) versus time constant of photostimulation group (τ_{pg}). **d**, τ_{pg} versus average selectivity of the directly photostimulated neurons (Methods). **c**,**d**, Error bars, s.e.m.; $n = 215$ photostimulation groups, 8 mice. AU, arbitrary units.

distance from the photostimuli (Fig. 2a) (length constant, 40 μm). Additional coupled neurons were presumably outside the FOV.

Like-to-like functional connectivity between ALM. Photostimuli caused transient increases in activity with diverse amplitudes and dynamics (Fig. 1e). On average, photostimulation increased the activity of targeted (Fig. 1e) and directly photostimulated (Fig. 1f) neurons for several seconds (mean, $\tau_{pg} = 3.1$ s; range, 2.0–4.6 s, 75% CI). The persistence of responses was much longer than the decay of GCaMP6s fluorescence expected after a short burst of activity[21] ($\tau_{GCaMP6s} = 1.1$ s, Fig. 2b, green line, and Extended Data Fig. 5). Coupled neurons also had decay times that were longer than $\tau_{GCaMP6s}$, and correlated with τ_{pg} (Fig. 2c; Pearson's correlation = 0.49, $P < 10^{-5}$). τ_{pg} values were longest when the directly photostimulated population was selective for rightward licking (Fig. 2d; Pearson's correlation = 0.35, $P = 3 \times 10^{-7}$). In summary, photostimulation of small groups of neurons changed activity in sparse populations of coupled neurons, and these changes in activity outlasted the photostimuli by several seconds.

Persistent activity is thought to be generated by recurrent connections between neurons with similar tuning[5,14,25]. We tested for specificity in functional connectivity by analyzing the responses of coupled neurons. We first analyzed photostimulated and coupled neurons based on their selectivity in trials without photostimulation. We grouped experiments in which the directly photostimulated population was mostly right selective (R) (Fig. 3a, top) or left selective (L) (Fig. 3a, bottom) and then analyzed separately the responses of coupled R and L neurons (Fig. 3a, right). Responses were stronger in coupled R neurons when R neurons were photostimulated, consistent with elevated like-to-like connectivity (Fig. 3b and Extended Data Fig. 6, blue line; Pearson's correlation = 0.27, $P = 7 \times 10^{-5}$). However, coupled L neurons responded weakly to photostimulation of both R and L neurons (Fig. 3b, red line; $P = 0.42$). These findings are consistent with previous experiments showing larger noise correlations in spiking between R neurons

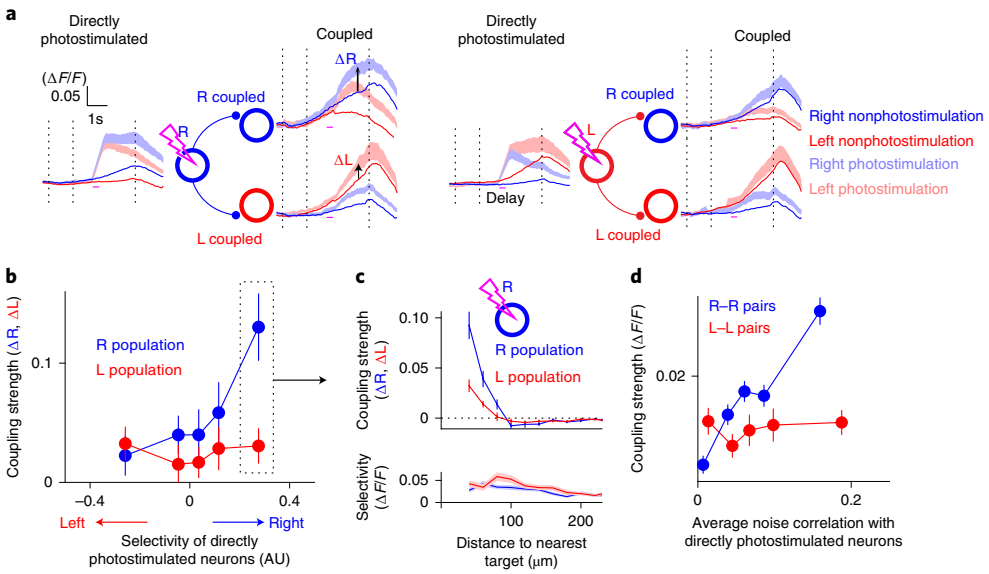

Fig. 3 | Functional connectivity depends on response type. a, Analysis of functional connectivity. Left: activity averaged across right-selective (top; R, blue circle) and left-selective (bottom; L, red circle) photostimulation groups (70 each; correct trials only). Dashed vertical lines denote the sample, delay and response epochs. Right: activity of coupled R or L populations. Traces: average activity of all coupled R- or L-selective neurons (30–100 μm from nearest target) weighted by the strength of their selectivity (S_i^{norm}; Methods). Arrows show calculation of coupling strength on to the L population (ΔL, Methods); calculation of ΔR is similar and based on R-coupled neurons. **b**, Coupling strength (ΔR and ΔL, calculated with both correct and incorrect trials) versus average selectivity of directly photostimulated neurons (Fig. 1f). Data were binned in quintiles along the *x* axis. AU, arbitrary units. **c**, Top: coupling strength (ΔR and ΔL) in response to photostimulation of R neurons versus distance to nearest photostimulation target (corresponding to dashed box in **b**). Bottom: average selectivity of coupled R and L populations versus distance to nearest photostimulation target. (error shade, s.e.m.). **d**, Coupling strength in each coupled R (blue) and L (red) neuron versus its average correlation with directly photostimulated R (blue) and L (red) neurons. **b**–**d**, Error bars, s.e.m. ($n = 215$ photostimulation groups, 8 mice).

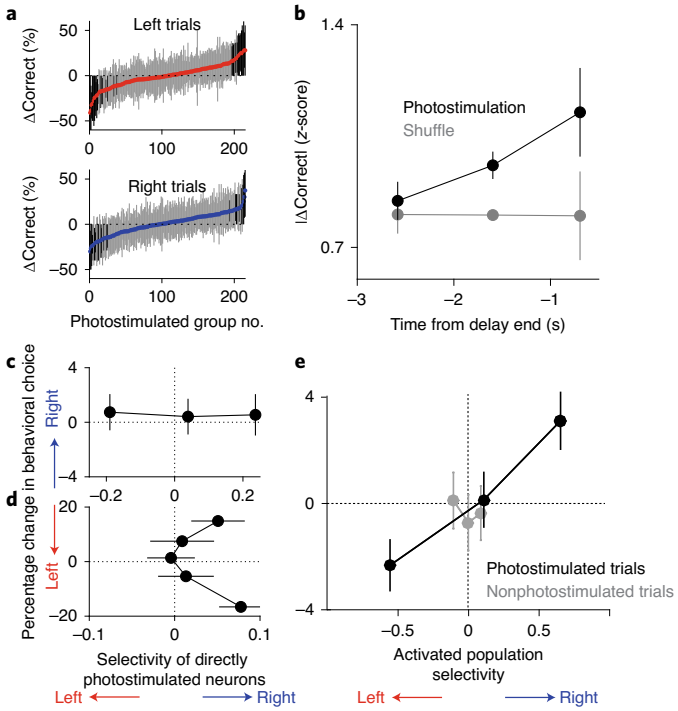

Fig. 4 | Photostimulation causes predictable changes in behavior. **a**, Change in behavioral performance between photostimulation and nonphotostimulation trials for each photostimulation group for left (top) and right (bottom) trials. Bars are 95% CIs of the bootstrap and dots are the mean. Black bars are all photostimulated groups with $P < 0.05$. Top and bottom were sorted independently. **b**, Absolute value of the change in correct rate normalized by the s.d. of the bootstrap distributions (**a**) versus time of photostimulation relative to the onset of the go cue. **c**, Change in percentage of right licking versus selectivity of targeted neurons. Data were binned in tertiles along the *x* axis. **d**, Change in percentage of right licking versus selectivity of targeted neurons. Data were binned in quintiles along the *y* axis. **e**, Change in percentage of right licking versus activated population selectivity (error bars, s.e.m.; $n = 215$ photostimulation groups, 8 mice).

than between L neurons[15]. The like-to-like excitation from R neurons decreased steeply with distance (Fig. 3c, top), even though selective neurons were present throughout the FOV (Fig. 3c, bottom). These results suggest that recurrent excitation between sparse subsets of nearby R neurons (that is, neurons selective for contralateral movements) contribute to maintenance of persistent activity. Covariations in pairwise trial-to-trial variability (noise correlations) are thought to reflect connectivity. We found that R neurons that were most correlated with the directly photostimulated R populations had stronger coupling (Fig. 3d, blue line; Pearson's correlation = 0.08, $P < 10^{-5}$), whereas noise correlations between L neurons were not predictive of coupling strength (Fig. 3d, red line; Pearson's correlation = 0.01, $P = 0.36$). This result suggests that noise correlations between R neurons are caused by coupling locally within the cortex, whereas noise correlations between L neurons reflect common inputs, potentially from the contralateral hemisphere[14].

Targeted photostimulation causes behavioral biases. Selective delay epoch activity of ALM neural populations is causally linked to the direction of future licking[14]. As targeted photostimuli produced changes in delay epoch activity that persisted until movement onset, we tested for effects on animal behavior. A substantial proportion of photostimulation groups produced changes in behavior ($P < 0.05$, bootstrap; 22/215 and 35/215 photostimulation groups on right and left trials, respectively) (Fig. 4a), approximately twofold greater than expected by chance (Extended Data Fig. 7, $P < 0.001$, Kolmogorov–Smirnov test; Methods). Previous studies have observed behavioral changes with manipulation of a similar number of neurons[26–28]. The behavioral biases were larger for later photostimuli (Fig. 4b; Pearson's correlation = 0.12, $P = 0.01$), with a time course that was similar to the decay of photostimulation-triggered activity (Extended Data Fig. 5).

The direction of bias was not correlated with the selectivity of the directly photostimulated (Fig. 4c; Pearson's correlation = −0.03, $P = 0.61$) or targeted (Pearson's correlation = −0.03, $P = 0.59$) populations. Surprisingly, when aggregating photostimulation groups based on behavioral effect, both left and right behavioral biases occurred when the directly photostimulated neurons were R selective on average (Fig. 4d). Similar results were obtained with larger photostimulation groups (25 neurons per group; Extended Data Fig. 7h).

To begin to explain this unexpected result we compared behavior with the net selectivity change caused by the photostimulation group across all neurons in the FOV, including coupled neurons. For each imaged neuron we separately calculated the average photostimulated change in activity and the average selectivity. We then defined the 'activated population selectivity' as the product of these two quantities, summed across the population (Extended Data Fig. 7). Bias in lick direction was correlated with activated population selectivity calculated across all neurons in the FOV (Fig. 4e, black line; Pearson's correlation = 0.10, $P < 0.01$). This effect was not due to a general correlation between population activity and behavior, because performing a similar analysis on nonphotostimulation trials did not yield a correlation (Fig. 4e, gray line). We conclude that targeted photostimulation of a small proportion of ALM neurons during the delay epoch produced predictable effects on neural activity and behavior.

Modular attractor network model of short-term memory. Measurements of neural activity in groups of neurons imposes incomplete constraints on network connectivity[29]. In contrast, our targeted photostimulation produced constraints that require major updates to widely used models of short-term memory. Common low-dimensional attractor models of persistent activity[5] contain a single persistent mode of activity. Therefore, perturbations in these models cause either persistent activity in all neurons or activity in none of the neurons (Extended Data Fig. 8). In contrast, different photostimulation groups often produced persistent changes in largely nonoverlapping subpopulations of R neurons (Fig. 5a–f).

We constructed model networks that produce activity consistent with the data (Fig. 5g,i). Sparse and selective activation after photostimulation implies sparse connectivity between model R neurons. The persistent activity after photostimulation requires strong recurrent interactions within these sparse subnetworks.

To test further whether this modular architecture is consistent with targeted photostimulation experiments, we fit[30] model networks directly to the population recordings in photostimulated and nonphotostimulated trials (Fig. 5i). The resultant inferred networks were biased toward local connectivity (Fig. 5j), reflecting the length scale of the photostimulation response (Figs. 2a and 3c) and local cortical connectivity[16,18]. Connections between R neurons were stronger than connections between L neurons (Fig. 5j), enabling the inferred networks to produce longer timescale responses to photostimulation of R neurons than L neurons (Fig. 2d). Analysis of the local connectivity revealed that the inferred networks resemble the modular network in Fig. 5g (Extended Data Fig. 8). Networks trained to match only the nonphotostimulation trials exhibited substantially weaker connections that resembled the nonmodular network (Fig. 5h), demonstrating the power of perturbation experiments to constrain neural network models. Note that these models

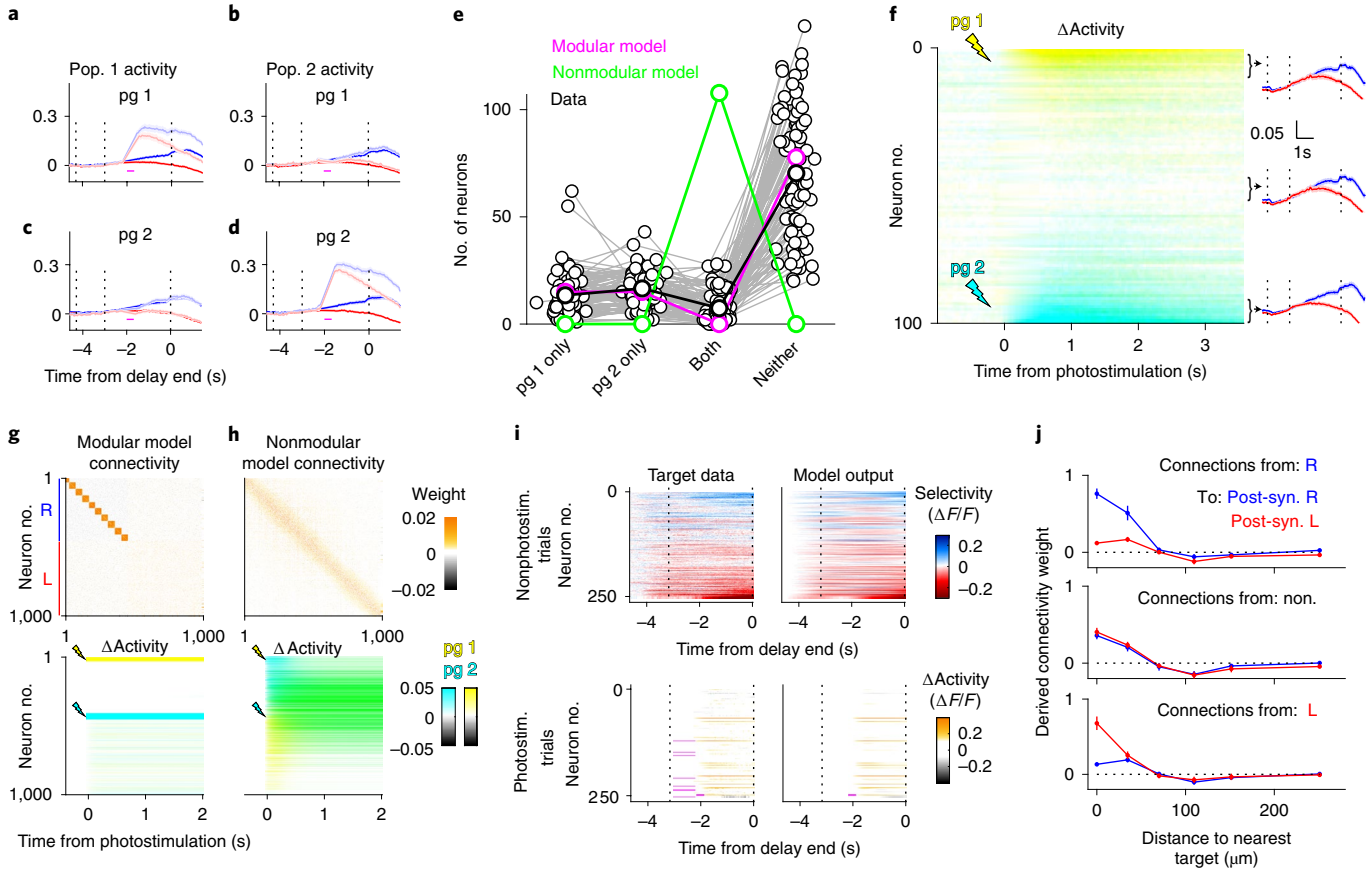

Fig. 5 | Modular network architecture can explain sparse and persistent photostimulation responses. a–d, Noninteracting subpopulations of R neurons. Response of population 1 (pop. 1; **a**) and population 2 (pop. 2; **b**) to pg 1 and pop. 2 (**c**) and pop. 1 (**d**) to pg 2. **e**, Number of R neurons excited by: pg 1 only, pg 2 only, both pg 1 and pg 2, or neither. Points are data from individual sessions. Magenta indicates numbers of neurons excited in a modular network model (**g**). Green indicates the number of neurons excited in a nonmodular network model (**h**). **f**, ΔActivity of all R-selective neurons in response to pg 1 (yellow) and pg 2 (cyan). Note the absence of neurons excited by pg 1 and pg 2 (green). Traces are nonphotostimulation activity of neurons with the largest (top and bottom) and smallest (middle) photostimulation responses. Lightning bolts are timing and location of photostimulation. **g**,**h**, Connectivity (top) and response to targeted photostimulation (bottom) of model networks with locally biased connectivity with modular (**g**) and nonmodular (**h**) organization; note the neurons excited by pg 1 and pg 2 (green). Model neurons were sorted according to spatial location. **i**, Data-driven inference of connectivity. Model network connections were tuned to match the model output (right panels) to the recorded data (left panels). Top row: activity on left trials subtracted from activity on right trials (selectivity) for each neuron. Dashed lines are the sample and delay epochs. Magenta lines are the timing and location of photostimulation. **j**, Connection weights from presynaptic R (top panel), nonselective (middle panel) and L (bottom panel) neurons on to postsynaptic (Post-syn.) R (blue) and L (red) neurons as a function of distance between neurons (error bars, s.e.m.; $n = 215$ photostimulation groups, 8 mice).

ascribe modularity to the local cortical connections, but modularity in multilaminar and multiregional networks, such as the corticothalamocortical loop, could also contribute to our findings[31] (Extended Data Fig. 8).

Modules are coupled through weak and random inhibition (Fig. 6a and Extended Data Fig. 8j). Because many modules coexist, the network is sparse and high-dimensional. L neurons were weakly coupled and inherited selectivity from long-range inputs (Fig. 3d). As the task is symmetric, we assume that right ALM contains strongly coupled L neurons, which project to the left hemisphere and right ALM, and thus could be the source of this drive.

As in the data, in the modular network different photostimulation groups triggered persistent responses in distinct groups of coupled neurons. In contrast, these photostimulation groups caused overlapping activation in models lacking the modular architecture (Fig. 5h). Model responses produced the counterintuitive behavioral effects of perturbation (Fig. 4d): stimulating R neurons could cause either left- or right-activated population selectivity. This occurred in the model because activated R modules sometimes inhibit other R modules to produce overall left bias in the neural population and behavior (Fig. 6b and Extended Data Fig. 9).

Discussion

Transient perturbations of small groups of neurons caused long-lasting network responses, modifying the state of a neural circuit for decision-making and modulating behavior seconds later. The responses were limited to a sparse subset of neurons with a particular selectivity. We propose a model network composed of strongly connected subnetworks, or 'modules'[32], that independently produce persistent activity. Strongly connected subnetworks have been reported based on analysis of connectivity in cortical brain slices[20] and have been proposed to underlie slow network dynamics[33]. Unlike nonmodular attractor networks, in which low-dimensional activity is a consequence of network-wide coupling, activity in our modular network model is low dimensional because each module receives similar external input during the sample epoch. The modules probably include deep-layer ALM and thalamic[31] neurons, which were coupled to the photostimulated

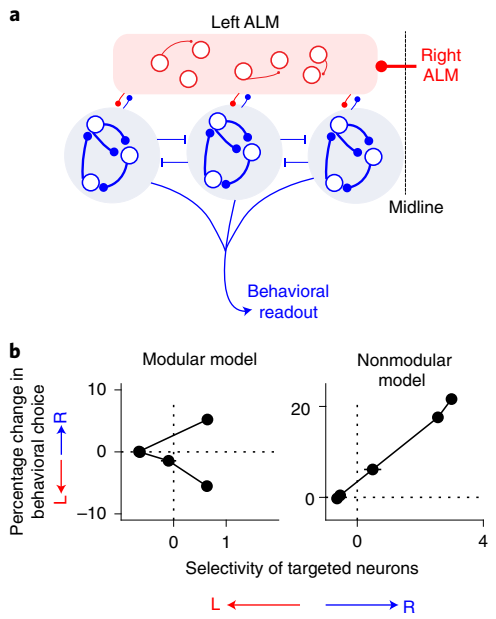

Fig. 6 | Behavioral biases in a modular network. a, Network with within-module (blue neurons) excitation and between-module inhibition. Behavioral choice was uniformly read out from all modules. **b**, Fractional change of right licking versus selectivity of targeted neurons for a modular network (left panel) and a nonmodular network (right panel). Data were binned in quintiles along the *x* axis (error bars, s.e.m.; 100 simulated photostimulation groups, 10 neurons per group).

neurons but were not recorded in our experiments. We hypothesize that the modular organization may be less sensitive to noise than line-attractor networks, and provide for higher memory capacity than standard discrete attractor networks.

Photostimulation of some groups of R neurons drove rightward behavioral biases, whereas other groups of R neurons drove leftward biases. This complex relationship between selectivity of the photostimulated population and behavioral bias contrasts with views of neural coding in which task-related selectivity can be interpreted as an accurate proxy for a neuron's contribution to behavior[14,34]. Instead, an accurate account of a neuron's influence on behavior requires characterization of its coupling to other neurons. Although most R neurons drove rightward selectivity in neighboring neurons (within 100 µm, Fig. 3c), long-range coupling was more heterogeneous, including R neurons driving leftward selectivity. When these network-wide interactions are considered via the activated population selectivity, we were able to predict the bias produced by a specific manipulation (Fig. 4e). In the modular attractor model, heterogeneous connectivity between modules recapitulates the counterintuitive relationship between selectivity of the directly photostimulated neurons and behavioral bias (Fig. 6b). Intermodule connectivity can be tuned to enhance the dynamic range of memory encoding and reduce sensitivity to noise[35,36].

Targeted photostimulations of a few neurons early in the delay epoch causes behavioral biases seconds later; in contrast, network-wide photoinhibition has revealed robustness of ALM activity network wide[14,25]. This discrepancy could be reconciled by a network with connectivity within modules producing attractor energy surfaces with flat troughs, whereas intermodular connections could produce global alignment of modules into more discrete states associated with each behavioral choice (right versus left). In addition, strong, network-wide perturbations could selectively engage intermodular dynamics or nonlinear interactions in large-scale circuits (for example, thalamocortical interactions[31]; Extended Data Fig. 10). These questions motivate future experiments in which larger numbers of neurons can be photostimulated[37–39] over larger length scales.

Online content

Any methods, additional references, Nature Research reporting summaries, extended data, supplementary information, acknowledgements, peer review information; details of author contributions and competing interests; and statements of data and code availability are available at https://doi.org/10.1038/s41593-020-00776-3.

Received: 12 August 2020; Accepted: 15 December 2020;
Published online: 25 January 2021

References

1. Romo, R., Brody, C. D., Hernández, A. & Lemus, L. Neuronal correlates of parametric working memory in the prefrontal cortex. *Nature* **399**, 470–473 (1999).
2. Fuster, J. M. & Alexander, G. E. Neuron activity related to short-term memory. *Science* **173**, 652–654 (1971).
3. Guo, Z. V. et al. Flow of cortical activity underlying a tactile decision in mice. *Neuron* **81**, 179–194 (2014).
4. Cannon, S. C., Robinson, D. A. & Shamma, S. A proposed neural network for the integrator of the oculomotor system. *Biol. Cybern.* **49**, 127–136 (1983).
5. Seung, H. S. How the brain keeps the eyes still. *Proc. Natl Acad. Sci. USA* **93**, 13339–13344 (1996).
6. Goldman, M. S. Memory without feedback in a neural network. *Neuron* **61**, 621–634 (2009).
7. Lim, S. & Goldman, M. S. Balanced cortical microcircuitry for maintaining information in working memory. *Nat. Neurosci.* **16**, 1306–1314 (2013).
8. Chaudhuri, R. & Fiete, I. Computational principles of memory. *Nat. Neurosci.* **19**, 394–403 (2016).
9. Wang, X.-J. Synaptic reverberation underlying mnemonic persistent activity. *Trends Neurosci.* **24**, 455–463 (2001).
10. Machens, C. K., Romo, R. & Brody, C. D. Functional, but not anatomical, separation of 'what' and 'when' in prefrontal cortex. *J. Neurosci.* **30**, 350–360 (2010).
11. Kaufman, M. T., Churchland, M. M., Ryu, S. I. & Shenoy, K. V. Cortical activity in the null space: permitting preparation without movement. *Nat. Neurosci.* **17**, 440–448 (2014).
12. Fisher, D., Olasagasti, I., Tank, D. W., Aksay, E. R. F. & Goldman, M. S. A modeling framework for deriving the structural and functional architecture of a short-term memory microcircuit. *Neuron* **79**, 987–1000 (2013).
13. Das, A. & Fiete, I. R. Systematic errors in connectivity inferred from activity in strongly recurrent networks. *Nat. Neurosci.* **23**, 1286–1296 (2020).
14. Li, N., Daie, K., Svoboda, K. & Druckmann, S. Robust neuronal dynamics in premotor cortex during motor planning. *Nature* **532**, 459–464 (2016).
15. Inagaki, H. K., Inagaki, M., Romani, S. & Svoboda, K. Low-dimensional and monotonic preparatory activity in mouse anterior lateral motor cortex. *J. Neurosci.* **38**, 4163–4185 (2018).
16. Holmgren, C., Harkany, T., Svennenfors, B. & Zilberter, Y. Pyramidal cell communication within local networks in layer 2/3 of rat neocortex. *J. Physiol.* **551**, 139–153 (2003).
17. Chettih, S. N. & Harvey, C. D. Single-neuron perturbations reveal feature-specific competition in V1. *Nature* **567**, 334–340 (2019).
18. Peron, S. et al. Recurrent interactions in local cortical circuits. *Nature* **579**, 256–259 (2020).
19. Song, S., Sjöström, P. J., Reigl, M., Nelson, S. & Chklovskii, D. B. Highly nonrandom features of synaptic connectivity in local cortical circuits. *PLoS Biol.* **3**, e68 (2005).
20. Perin, R., Berger, T. K. & Markram, H. A synaptic organizing principle for cortical neuronal groups. *Proc. Natl Acad. Sci. USA* **108**, 5419–5424 (2011).
21. Chen, T.-W. et al. Ultrasensitive fluorescent proteins for imaging neuronal activity. *Nature* **499**, 295–300 (2013).
22. Klapoetke, N. C. et al. Independent optical excitation of distinct neural populations. *Nat. Meth.* **11**, 338–346 (2014).
23. Chen, T.-W., Li, N., Daie, K. & Svoboda, K. A map of anticipatory activity in mouse motor cortex. *Neuron* **94**, 866–879.e4 (2017).
24. Li, N., Chen, T.-W., Guo, Z. V., Gerfen, C. R. & Svoboda, K. A motor cortex circuit for motor planning and movement. *Nature* **519**, 51–56 (2015).
25. Inagaki, H. K., Fontolan, L., Romani, S. & Svoboda, K. Discrete attractor dynamics underlies persistent activity in the frontal cortex. *Nature* **566**, 212 (2019).

26. Tanke, N., Borst, J. G. G. & Houweling, A. R. Single-cell stimulation in barrel cortex influences psychophysical detection performance. *J. Neurosci.* **38**, 2057–2068 (2018).
27. Huber, D. et al. Sparse optical microstimulation in barrel cortex drives learned behaviour in freely moving mice. *Nature* **451**, 61–64 (2008).
28. Jennings, J. H. et al. Interacting neural ensembles in orbitofrontal cortex for social and feeding behaviour. *Nature* **565**, 645–649 (2019).
29. Denk, W., Briggman, K. L. & Helmstaedter, M. Structural neurobiology: missing link to a mechanistic understanding of neural computation. *Nat. Rev. Neurosci.* **13**, 351–358 (2012).
30. Rajan, K., Harvey, C. D. & Tank, D. W. Recurrent network models of sequence generation and memory. *Neuron* **90**, 128–142 (2016).
31. Guo, Z. V. et al. Maintenance of persistent activity in a frontal thalamocortical loop. *Nature* **545**, 181–186 (2017).
32. Newman, M. E. J. Modularity and community structure in networks. *Proc. Natl Acad. Sci. USA* **103**, 8577–8582 (2006).
33. Litwin-Kumar, A. & Doiron, B. Slow dynamics and high variability in balanced cortical networks with clustered connections. *Nat. Neurosci.* **15**, 1498–1505 (2012).
34. Britten, K. H., Newsome, W. T., Shadlen, M. N., Celebrini, S. & Movshon, J. A. A relationship between behavioral choice and the visual responses of neurons in macaque MT. *Vis. Neurosci.* **13**, 87–100 (1996).
35. Mosheiff, N. & Burak, Y. Velocity coupling of grid cell modules enables stable embedding of a low dimensional variable in a high dimensional neural attractor. *Elife* **8**, e48494 (2019).
36. Chaudhuri, R. & Fiete, I. in *Advances in Neural Information Processing Systems* (eds Wallach, H. et al.) 7688–7699 (Curran Associates, Inc., 2019).
37. Marshel, J. H. et al. Cortical layer-specific critical dynamics triggering perception. *Science* **365**, eaaw5202 (2019).
38. Mardinly, A. R. et al. Precise multimodal optical control of neural ensemble activity. *Nat. Neurosci.* **21**, 881–893 (2018).
39. Yang, W., Carrillo-Reid, L., Bando, Y., Peterka, D. S. & Yuste, R. Simultaneous two-photon imaging and two-photon optogenetics of cortical circuits in three dimensions. *Elife* **7**, e32671 (2018).

Publisher's note Springer Nature remains neutral with regard to jurisdictional claims in published maps and institutional affiliations.

© The Author(s), under exclusive licence to Springer Nature America, Inc. 2021

Methods

Mice. Data are from 15 mice (age at the beginning of experiments, 70–150 d); 12 mice were used for photostimulation during behavior, 2 were used for characterization of the spatial resolution of photostimulation (Fig. 1c and Extended Data Fig. 4) and 1 for electrophysiology (Extended Data Fig. 3). All mice were CamK2a-tTA (JAX, catalog no. 007004) × Ai94 (TITL-GCaMP6s)[40] (JAX, catalog no. 024104). Half of the mice were crossed with Emx1-Cre (JAX, catalog no. 005628) and the other half with slc17a7 IRES Cre (JAX, catalog no. 023527), both providing widespread expression of GCaMP6s in excitatory cortical neurons.

Surgical procedures. All procedures were in accordance with protocols approved by the Janelia Institutional Animal Care and Use Committee. Cranial window surgeries were performed as described previously (https://www.protocols.io/private/40BDB9040AA0706D61C7F4D6B200C194). During surgical procedures mice were anesthetized using 1–2% Isoflurane. After surgery mice were given buprenorphine-HCl (0.1 ml, 0.03 mg ml^{-1}). Ketoprofen (0.1 ml, 0.1 mg ml^{-1}) was provided on the day of surgery and for 2 d after surgery. Then 3-mm circular craniotomies were centered over ALM (2.5 mm anterior and 1.5 mm lateral from Bregma). Virus (10^{12} titers; AAV2/2 camKII-KV2.1-ChrimsonR-FusionRed; Addgene, plasmid catalog no. 102771) was injected 400 µm below the dura (4–10 sites, 20–30 nl each, or 2 sites, 100 nl each), centered within the craniotomy and spaced by 500 µm. The craniotomy was covered by a cranial window composed of three layers of circular glass (total thickness 450 µm). The diameter of the bottom two layers was 2.5 mm. The top layer was 3 mm or 3.5 mm and rested on the skull. The window was cemented in place using cyanoacrylate glue and dental acrylic (Lang Dental). A customized headbar was attached just anterior to the window using cyanoacrylate glue and dental cement. After 3–7 d of recovery mice were placed on water restriction (1 ml d^{-1}) in a reverse light cycle room. Behavioral training started 3–5 d later. Coexpression of GCaMP6s and ChrimsonR was confirmed in histological sections imaged using an inverted confocal microscope (Extended Data Fig. 1; Zeiss, LSM 880 Airyscan).

Behavior. Behavioral training was performed using methods and software (http://brodylab.princeton.edu/bcontrol) described previously[15,41]. Briefly, mice were presented with one of two auditory cues. Half of the mice were trained to discriminate between 3-kHz and 12-kHz pure tones, and the other half were trained to discriminate between white noise and an equally weighted combination of pure tones with frequencies of 0.5, 1, 2, 4, 8 and 16 kHz. No qualitative differences in ALM activity resulted from using different sets of auditory stimuli. During the sample epoch (1.25 s) white noise was played continuously, whereas tones were played for five repetitions of 150-ms pulses with 100-ms interpulse intervals. During the sample and delay epochs, the lickports were out of reach of the mouse[42]. The lickports began moving toward the mouse 2.6 s after the start of the delay, arriving 3 s after the start of the delay. The arrival of the lickport served as a 'go cue' for the mice to begin licking. Mice were allowed to lick for reward 3 s after the start of the delay epoch.

Imaging and photostimulation experiments began once the mice achieved performance of >65%, typically 4–6 weeks after the start of training. Statistical power analysis revealed that 65% performance maximizes our ability to detect changes in behavior caused by photostimulation. An exploratory round of experiments (3 mice, 33 sessions), in which 4 or 5 groups were photostimulated per experiment, showed small but robust changes in mouse behavior after photostimulation. Based on these preliminary experiments, in the second round of experiments we enhanced our ability to detect changes in behavior by increasing the number of trials per photostimulation group (5 mice, 51 sessions) at the expense of the number of photostimulation groups (2 per session). Given the number of photostimulation trials per session (mean, 25; range, 13–38, 75% CI, per trial type), statistical power analysis indicated that behavioral changes >±18% correspond to $P<0.05$ in single sessions.

Microscope. Two-photon imaging and two-photon photostimulation were performed using a customized microscope[42] with a photostimulation path, which consisted of a 1,040-nm pulsed laser (Fidelity 10, Coherent), a Pockels cell (Conoptics) for power modulation, and a pair of galvanometer mirrors (Cambridge, 6215H) for beam positioning (Extended Data Fig. 1). Imaging was with 920-nm light (Chameleon Ultra II, Coherent) and a resonant scanner (Thorlabs). Imaging and photostimulation were controlled by Scanimage 2016a (Vidrio).

The FOV was adjusted according to the spatial range of opsin expression (one of: (1) 585 × 599 µm^2, 512 × 512 pixels^2, 30 Hz; (2) 814 × 32 µm^2, 640 × 640 pixels^2, 24 Hz; and (3) 968 × 822 µm^2, 700 × 700 pixels^2, 22 Hz). Imaging was restricted to the most superficial plane in layer 2/3 of the anterolateral motor cortex that contained a high density of GCaMP6s- and ChrimsonR-expressing neurons (typically 150 µm from brain surface, range, 125–250 µm).

Volumetric imaging was performed in a subset of mice in 4 ($n=3$ mice) or 5 ($n=1$ mice), 350 × 310 µm^2 (300 × 300 pixels^2) FOVs each separated by 40 µm along the axial dimension. Planes were imaged sequentially by adjusting the electric tunable lens and blanking acquisition for 14 ms between frames to allow the lens to settle, resulting in imaging rates of 7.59 and 6.07 Hz for 4- and 5-plane volumes. Photostimuli were located in the most superficial plane.

Photostimulation and behavior experiments. Neurons were chosen for membership in a photostimulation group based on their selectivity. Selectivity of individual neurons was determined based on either activity in the first 30–70 trials in a session or activity measured on the previous day. We prioritized selection of neurons with selectivity in the last 0.5 s of the delay epoch and/or the first 0.5 s of the response epoch. Selectivity in layer 2/3 is sparse, increasing during the delay epoch and peaking just after the go cue (Extended Data Fig. 2). We therefore selected neurons with late delay and/or early response selectivity. Late-delay and early-response activity was highly correlated, in part because of the slow kinetics of GCaMP6s. For consistency, we included both late-delay and early-response selectivity in our analysis throughout the paper. However, if we restrict our definition of selectivity to include only late-delay activity, the main results of the paper remain the same (data not shown). Previous work has shown that activation of individual cortical neurons produced changes in coupled neurons that are too small to be detected with our limited number of behavioral trials[17,43]. To increase the likelihood of detecting coupled neurons we photostimulated groups of eight neurons. As the average FOV contained 20 selective neurons on average, photostimulation of 8 neurons still left a sufficient number of nonphotostimulated selective neurons to observe connectivity based on selectivity (for example, 'like to like'). In experiments without eight late delay/early response selective neurons, we included neurons that were selective during the early delay or sample epochs or nonselective neurons. After defining two to five photostimulation groups for a session, the photostimulation targets were loaded into ScanImage using customized Matlab software. Each neuron was photostimulated for 3 ms each, with 1 ms between photostimulation of different neurons (Extended Data Fig. 3). After all eight neurons had been photostimulated (8 × (3 ms + 1 ms) = 32 ms), the first neuron was photostimulated again until each neuron was photostimulated ten times, for a total of 10 × 32 ms = 320 ms. The power of the photostimulation beam at the sample was 100–150 mW. As this power was sufficient to excite GCaMP fluorescence, all imaging frames acquired during the photostimulation were discarded. Photostimuli were typically provided 1 s after the start of the delay epoch (138/215 photostimulation groups), but, in some experiments we photostimulated 1 s earlier (61/215 groups) or later (16/215 groups). Photostimulation and control trials were randomly interleaved, with photostimuli delivered on either 33% or 40% of trials. Data collection and analysis were not performed blind to the conditions of the experiments.

Electrophysiology. Extracellular voltage was recorded in cell-attached mode in a lightly anesthetized mouse (0.75% isoflurane). Signals were acquired using an Axopatch 700B amplifier (Molecular Devices) at 20 kHz (http://wavesurfer.janelia.org). Electrodes with 10-MΩ impedance were filled with artificial cerebrospinal fluid (in mM): 125 NaCl, 5 KCl, 10 dextrose, 10 4-(2-hydroxyethyl)-1-piperazine-ethanesulfonic acid, 2 $CaCl_2$, 2 $MgSO_4$, pH 7.4; they were then advanced toward a neuron of interest in layer 2/3 of primary motor cortex with 6,900 Pa of positive pressure. Neurons were photostimulated with a train of 10 3-ms spirals with a 28-ms interspiral interval at 50, 100 and 150 mW.

Analysis of calcium-related fluorescence dynamics. Regions of interest corresponding to cell bodies were generated using a semi-automated algorithm[21]. Cell bodies were identified in images averaged across a session, and images in which all frames corresponding to correct lick-left trials were averaged and subtracted from an average of all frames from correct lick-right trials. These selectivity maps (Extended Data Fig. 2a) were used to choose neurons for photostimulation and also to ensure that all selective neurons were included in the analysis. Activity, $f(t) = \Delta F(t)/F_0$, was calculated for each cell by defining baseline fluorescence (F_0) as the average fluorescence during the pre-sample period averaged across all trials. Fluorescence traces were then separated by trial type. The fluorescence trace at time t of neuron i on trial number j, trial type k (left, $k=$L; right, $k=$R; both left and right, $k=$L&R) and photostimulation group no. s (nonphotostimulation, $s=$non.; photostimulation of group pg, $s=$pg) is $f_{i,j}^{k,s}(t)$. In this notation the activity of neuron i on the jth lick-right trial with photostimulation of group pg is $f_{i,j}^{R,\mathrm{pg}}$.

Selectivity. Selectivity for trial type was used to choose neurons for photostimulation and to group neurons for analysis. Selectivity, S_i, is the trial-averaged difference between fluorescence for left- and right-correct nonphotostimulation trials, around the go cue (t_{cue}):

$$S_i = \left\langle \langle f_{i,j}^{R,\mathrm{non.}}(t)\rangle_{j=\text{correct trials}} - \langle f_{i,j}^{L,\mathrm{non.}}(t)\rangle_{j=\text{correct trials}} \right\rangle_{t_{\mathrm{cue}}-0.5s>t>t_{\mathrm{cue}}+0.5s}$$

Change in activity caused by photostimulation. The trial-averaged change in activity produced by the photostimulation group pg on the ith neuron is (Δactivity, Fig. 1f):

$$\Delta_i^{\mathrm{L\&R,pg}}(t) = \langle f_{i,j}^{\mathrm{L\&R,pg}}(t)\rangle_{j=\text{all trials}} - \langle f_{i,j}^{\mathrm{L\&R,non.}}(t)\rangle_{j=\text{all trials}}$$

To characterize the strength of photostimulation in each neuron and trial (Fig. 2a), we compared the time-averaged fluorescence with and without photostimulation:

$$\bar{f}_{i,j}^{\mathrm{L\&R,pg}} = \langle f_{i,j}^{\mathrm{L\&R,pg}}(t)\rangle_{t_{\mathrm{pg}}<t<t_{\mathrm{pg}}+1s} \text{ and } \bar{f}_{i,j}^{\mathrm{L\&R,non.}} = \langle f_{i,j}^{\mathrm{L\&R,non.}}(t)\rangle_{t_{\mathrm{pg}}<t<t_{\mathrm{pg}}+1s}$$

where t_{pg} is the end of the photostimulus for group pg. P_i^{pg} is the P value (two-tailed Student's t-test) comparing the distributions of $\bar{f}_{i,j}^{\mathrm{L\&R,pg}}$ and $\bar{f}_{i,j}^{\mathrm{L\&R,non.}}$ for each neuron. We refer to all neurons that were within 20 µm of a photostimulation target with $P_i^{\mathrm{pg}} < 0.05$ as directly photostimulated. Neurons with $P_i^{\mathrm{pg}} < 0.05$ were plotted in Fig. 2a ('perturbed').

The average selectivity of all directly photostimulated neurons is $\sum_{D_i^{\mathrm{pg}}<20\mu m} S_i^{\mathrm{norm.}} \left\langle \Delta_i^{\mathrm{L\&R,pg}}(t)\right\rangle_{t_{\mathrm{pg}}<t<t_{\mathrm{pg}}+1s}$. D_i^{pg} is the distance of neuron i to the nearest photostimulation target in group pg (Figs. 2d and 3b, x axis). Here $S_i^{\mathrm{norm.}}$ is the average selectivity, S_i, divided by the s.d. in fluorescence of neuron i (z-scored), normalized to have R^2 norm = 1.

Persistence of activity after photostimulation. To quantify the persistence of the change in activity produced by photostimulation, we averaged the trial-averaged change in activity across all directly photostimulated neurons, $\langle \Delta_i^{\mathrm{L\&R,pg}}(t)\rangle_{i=\mathrm{direct}}$ (Fig. 2b). We define the decay time constant τ_{pg} as the time at which $\langle \Delta_i^{\mathrm{L\&R,pg}}(t)\rangle_{i=\mathrm{direct}}$ decays to 1/e of its peak value. As many photostimulation groups produce changes that remain larger than 1/e of the peak after 3 s, we fit $\langle \Delta_i^{\mathrm{L\&R,pg}}(t)\rangle_{i=\mathrm{direct}}$ using:

$$\left\langle \Delta_i^{\mathrm{L\&R,pg}}(t)\right\rangle_{i=\mathrm{direct}} = a\mathrm{e}^{-t/T_{\mathrm{decay}}}\left(1-\mathrm{e}^{-t/T_{\mathrm{rise}}}\right).$$

τ_{pg} is the time when the fit decayed to 1/e (Fig. 2b–d). Only photostimulation groups with photostimulation starting at 1 or 0 s after the start of the delay epoch (199 of 215 groups) were included in analysis of persistence. In Fig. 2c,d data were binned in quintiles based on their value along the x axis.

Relationship between directly photostimulated neurons and coupled neurons. The coupling strength from directly photostimulated neurons in group pg with neuron i was calculated as:

$$\text{Coupling strength}_i^{\mathrm{pg}} = \left\langle \Delta_i^{\mathrm{L\&R,pg}}(t)\right\rangle_{t_{\mathrm{pg}}<t<t_{\mathrm{pg}}+1s}$$

for all neurons >30 µm from a photostimulation target (Fig. 3b–d, y axes). Coupling in R (ΔR^{pg}) and L (ΔL^{pg}) populations was calculated as the average of the coupling strength for all R and L (Fig. 3b, y axis) neurons, where the contribution of each neuron was weighted by the normalized selectivity $S_i^{\mathrm{norm.}}$:

$$\Delta R^{\mathrm{pg}} = \left\langle \text{Coupling strength}_i^{\mathrm{pg}}\, S_i^{\mathrm{norm.}}\right\rangle_{i=\{D_i^{\mathrm{pg}}>30\mu m, S_i^{\mathrm{norm.}}>0\}}$$

$$\Delta L^{\mathrm{pg}} = \left\langle \text{Coupling strength}_i^{\mathrm{pg}}\, S_i^{\mathrm{norm.}}\right\rangle_{i=\{D_i^{\mathrm{pg}}>30\mu m, S_i^{\mathrm{norm.}}<0\}}.$$

$S_i^{\mathrm{norm.}}$ and $\text{Coupling strength}_i^{\mathrm{pg}}$ were computed by using nonoverlapping groups of randomly sampled nonphotostimulation trials. Data were binned in quintiles according to the selectivity of the directly photostimulated neurons (Fig. 3b, x axis). We further analyzed coupled responses to photostimulation of the groups with the strongest right selectivity (top quintile; Fig. 3b, dashed box). To assess the distance dependence of specific coupling, we calculated ΔR^{pg} and ΔL^{pg} in bins of 20-µm width from 30–250 µm (Fig. 3c, top). In these bins we also calculated the average normalized selectivity $S_i^{\mathrm{norm.}}$ (Fig. 3c, bottom).

We calculated the noise correlation (Fig. 3d) between two neurons i and j as:

$$C_{i,l}^{\mathrm{R}} = \left\langle \mathrm{Corr}\left(f_{i,j}^{\mathrm{R,non.}}(t) - \langle f_{i,j}^{\mathrm{R,non.}}(t)\rangle_{j=\text{all trials}}\ ,\ f_{l,j}^{\mathrm{R,non.}}(t) - \langle f_{l,j}^{\mathrm{R,non.}}(t)\rangle_{j=\text{all trials}}\right)\right\rangle_t.$$

The average correlation of coupled neuron i with photostimulation group pg was $C_i^{\mathrm{R,pg}} = \left\langle C_{i,l}^{\mathrm{R}}\right\rangle_{l=\mathrm{direct}}$. A similar analysis was performed for left trials. Noise correlations for right and left trials were then averaged (Fig. 3d, x axis):

$$\text{Avg. noise corr.} = C_i^{\mathrm{R,pg}}/2 + C_i^{\mathrm{L,pg}}/2.$$

We separately analyzed coupling strength versus average noise correlation for coupled R neurons ($S_i > 0$) when the selectivity of the directly photostimulated neurons was positive (Fig. 3d, blue line) and for coupled L neurons ($S_i < 0$) when the selectivity of the directly photostimulated neurons was negative (Fig. 3d, red line).

Changes in behavioral performance with photostimulation. For each photostimulation group, we calculated the difference in correct response rate between photostimulation trials and nonphotostimulation trials, separately for lick-left and lick-right trials. P values were calculated by downsampling the nonphotostimulation trials to match the number of photostimulation trials, 10,000 times with replacement (Fig. 4a and Extended Data Fig. 7). To estimate the false-positive rate, we calculated 10,000 null distributions of P values from the downsampled nonphotostimulation trials (Extended Data Fig. 7c) and compared this with the distribution of P values from photostimulation (Kolmogorov–Smirnov test).

To relate changes in behavior to photostimulated changes in activity, we plotted the change in behavioral choice versus the selectivity of directly photostimulated neurons (Fig. 4c,d). Data were binned in quintiles along either the x axis (Fig. 4c) or the y axis (Fig. 4d). Next, we calculated the 'activated population selectivity' (Extended Data Fig. 7; Methods) as the overlap between the photostimulated change in activity, $\langle \Delta_i^{\mathrm{L\&R,pg}}(t)\rangle_{t_{\mathrm{pg}}<t<t_{\mathrm{pg}}+0.5s}$, and trial-type selectivity, S_i. At the population level, the change in activity induced by photostimulation was relatively sparse (Figs. 1d and 5f) and trial-to-trial variability was substantial. We isolated the effects mediated by photostimulation from normal trial-to-trial variability. We first divided the photostimulation trials into two halves, a testing and training set. We next determined a photostimulation subspace $\mathbf{V}_{\mathrm{pg}}$ via singular value decomposition on half of the photostimulated data for time points immediately following photostimulation:

$$\langle \Delta_{i,\mathrm{train}}^{\mathrm{L\&R,pg}}(t)\rangle_{t_{\mathrm{pg}}<t} = \mathbf{USV}t_{\mathrm{train,pg}}.$$

where $\mathbf{U}$ and $\mathbf{V}$ are matrices of left and right singular vectors, and $\mathbf{S}$ is a diagonal matrix of singular values. We then projected the change in activity from the other half of the trials ($\langle \Delta_{i,\mathrm{test}}^{\mathrm{L\&R,pg}}(t)\rangle_{t_{\mathrm{pg}}<t<t_{\mathrm{pg}}+0.5s}$) on to this photostimulation subspace to obtain the photostimulation vector (Extended Data Fig. 7).

$$\text{Photostim. vector}^{\mathrm{pg}} = \sum_{m=1}^{M}\left(\Sigma_i V_{\mathrm{train},i,\mathrm{pg}}^m \langle \Delta_{i,\mathrm{test}}^{\mathrm{L\&R,pg}}(t)\rangle_{t_{\mathrm{pg}}<t<t_{\mathrm{pg}}+0.5s}\right) V_{\mathrm{train},i,\mathrm{pg}}^m$$

where the m denotes the mth column of $\mathbf{V}_{\mathrm{train,pg}}$. We limited analysis to the first mode of $\mathbf{V}_{\mathrm{pg}}$ (that is, $M = 1$) because it contained 93% of the root mean square signal of $\langle \Delta_{i,\mathrm{train}}^{\mathrm{L\&R,pg}}(t)\rangle_{t_{\mathrm{pg}}<t<t_{\mathrm{pg}}+0.5s}$. A qualitatively similar relationship between activated population selectivity and behavioral bias was observed for $M = 2$. Activated population selectivity (Fig. 4e, x axis) was calculated as:

$$\text{Activated pop. sel.}^{\mathrm{pg}} = \sum_i \text{Photostim. vector}_i^{\mathrm{pg}} S_i.$$

Random sampling of training and testing subsets was repeated ten times and the average activated population selectivity was computed for each photostimulation group. The same analysis was repeated by splitting nonphotostimulation trials into two nonoverlapping sets, and treating one set as if it were from a photostimulation experiment. This sham photostimulation subset was selected to have the same number of trials as the actual photostimulation experiment (Fig. 4e, gray), and was further split in half into randomly sampled training and testing subsets for ten repetitions, as described above for the actual photostimulation experiments.

Overlap of photostimulated activity. To quantify the degree to which distinct photostimulation groups produced excitation in overlapping populations (Fig. 5a–f) we calculated $\Delta_i^{\mathrm{L\&R,pg}}(t)$ for all R neurons in each session ($S_i > 0$) for pg 1 and pg 2. We sorted neurons based on the difference in their responses to pg 1 and pg 2 (Fig. 5f). To combine data across sessions with different numbers of R neurons (N_R; mean 107; range 51–158, 75% CI), $N_R \times$ T matrices (Fig. 5f) were linearly interpolated (Matlab, interp1) into 100 × T matrices and then averaged across sessions. For crossvalidation purposes unique subsets of trials were used for sorting and plotting. To further illustrate the lack of overlap, we found R neurons that responded only to pg 1 ($P < 0.1$, one-tailed Student's t-test), but not pg 2 ($P > 0.5$, one-tailed Student's t-test) and vice versa. Of the sessions 66% had multiple nonoverlapping populations consisting of at least three neurons each. Distributions of neurons responding only to pg 1 or pg 2, both pg 1 and pg 2 or neither pg 1 nor pg 2 were plotted in Fig. 5e. The crossvalidated average activity of these sessions that had both (1) a group of at least three neurons responding only to pg 1 and (2) a group of at least three neurons responding only to pg 2 are plotted in Fig. 5a–d.

Network models. The spike rate of model neuron i was determined by the equation:

$$\tau \dot{r}_i(t) = -r_i(t) + \Sigma_j w_{i,j} G(r_j(t)) + I_i(t)$$

where $w_{i,j}$ is the connection from neuron j on to neuron i, τ is the synaptic time constant (taken to be 100 ms), G is the synaptic nonlinearity and $I_i(t)$ is the external input. We constructed a modular network with 1,000 neurons, approximately equally divided between L and R neurons (Fig. 5g). The connection matrix W was composed of four components:

$$W = w_{\mathrm{module}} + w_{\mathrm{inter}} + w_{\mathrm{LL}} + w_{\mathrm{RL}}.$$

where w_{module} is within-module connectivity, w_{inter} the between-module connectivity, w_{LL} the connections between L neurons and w_{RL} the connections between R and L neurons. The number of neurons and spatial extent of modules were based on estimates of connectivity in local cortical circuits[20]. The recurrent connections within a module were made sufficiently strong to produce sparse persistent responses within the module (Fig. 5f). The network contained 10 nonoverlapping modules, each with 40–50 R neurons, but reasonably smaller or larger number of modules produced similar results. The remaining neurons were L neurons outside the modules. Assignment of neurons to modules was based on spatial structure. For simplicity, neurons were assigned a location along a single spatial dimension (Fig. 5g,h). Module centers, C_i, were uniformly distributed across this spatial dimension. Neurons were selected, without replacement, for

membership in the ith module with probability $P_i(x) = e^{-\sqrt{(x-C_i)^2}/200\,\mu m}$, so that each neuron belonged only to one module. Neurons not assigned to any module were included in the L population.

Connection probabilities and strengths varied across the four components. Connections between R and L neurons, w_{RL}, were sparse with 95% of connections set to zero. The value of the nonzero weights was drawn from a zero-mean Gaussian distribution with variance of 0.01. Connections within modules were dense with distance-dependent weights corresponding to $w_{\text{module};i,j} = e^{-\sqrt{(x_i-x_j)^2}/500\,\mu m}$. Connections between R neurons in different modules were sparse with 90% of connections set to zero. The value of nonzero weights was drawn from a uniform distribution with a range from $-1/M$ to 0, where the normalization M was calculated such that the largest eigenvalue of w_{inter} was 0.3. Connections between L neurons, w_{LL}, were sparse with 80% of connections randomly set to zero. The nonzero weights were distance dependent, $W_{LL;i,j} = 3e^{\sqrt{(x_i-x_j)^2}/70\,\mu m} - e^{\sqrt{(x_i-x_j)^2}/200\,\mu m}$, and were then scaled so that the maximum eigenvalue of w_{LL} was 0.7.

Neurons inside the modules (R neurons) received 100-ms sensory inputs with amplitude −0.1 on left trials and 0.1 on right trials. Neurons outside the modules (L neurons) inherit their persistent selectivity from the contralateral (right) hemisphere[14]. As the behavioral task is symmetric, we assume that the contralateral hemisphere also transforms a transient sensory input into a persistent selective output. Accordingly, the input from the right hemisphere is modeled as a persistent selective input with amplitude of 0.1 on left trials and −0.1 on right trials (Fig. 6a).

Brief (200 ms) photostimulation was provided to ten randomly selected neurons within one randomly selected module. We modeled the effect of photostimulation on behavior by the difference in activity on photostimulation and nonphotostimulation trials for all R neurons. This difference was normalized by the overall selectivity to estimate the behavioral bias:

$$\text{Behavioral bias} = \frac{\sum_{i=R_{neurons}} r_i^{L\&R,pg} - \sum_{i=R_{neurons}} r_i^{L\&R,non.}}{\sum_{i=R_{neurons}} r_i^{R,non.} - \sum_{i=R_{neurons}} r_i^{L,non.}}$$

where $r_i^{L\&R,pg}$ is the firing rate of neuron i on left and right trials in response to photostimulation group pg, and 'non.' corresponds to nonphotosimulated trials.

For the nonmodular network with local connectivity (Fig. 5h), 90% of connections were set to zero; nonzero connections were given by $w_{i,j} = e^{-|i-j|/200\,\mu m}$. For the nonmodular attractor models (where all neurons contribute to the attractor) (Extended Data Fig. 8a,b), w was a rank-one matrix constructed by taking the outer product of a Gaussian random 1,000 × 1 (mean 0; Euclidean norm 1) vector with itself. For the line-attractor model (Extended Data Fig. 8a), the synaptic function was $G(x) = x$; the discrete attractor model (Extended Data Fig. 8b) had $G(x) = 0.1\tanh(0.1x)$. Short-term memory was simulated by giving a brief (amplitude, 1 relative to sensory input amplitude; duration, 200 ms) input to each network along the network's primary eigenvector (eigenvalue = 1). Photostimulation was simulated by injecting a brief current to eight randomly chosen neurons.

Robust networks (Extended Data Fig. 10) achieved robustness to global photoinhibition through training of intermodular connections (Extended Data Fig. 10a–e; $G(r_i(t)) = \tanh(r_i(t))$ or discrete attractor dynamics ($G(r_i(t)) = \frac{1.4}{1+e^{-(r_i(t)-0.5)/0.3}}$; Extended Data Fig. 10f–j). For the modular model (Extended Data Fig. 10a–e), instead of modeling full networks, we coarse grained by modeling individual modules with 1-s synaptic time constants, that is, the slow dynamics is assumed to arise from strong within-module feedback, which is not modeled explicitly. The network was trained using the FORCE algorithm[44] to produce a persistent output along one dimension. On alternating training trials, broad transient photoinhibition was applied immediately after the sample epoch. Training sought to produce a change in activity along the persistent mode during photoinhibition, followed by a rapid recovery after the offset of photoinhibition, as seen in experiments[15]. In the hybrid discrete/continuous attractor model (Extended Data Fig. 10f–j), a fine-tuned approximately linear transfer function $f(x) = \frac{1.4}{1+e^{-(x-0.5)/0.3}}$ coupled with self-exciting and mutually inhibiting L (red) and R (blue) neurons produces slow dynamics along the difference mode [1, −1] and fast dynamics along the [1, 1] direction.

Generating model connectivity by fitting to data. Connectivity matrices were trained to fit the activity of all individual neurons[30]. For each experimental session with N recorded neurons we fit the $N \times N$ matrix $w_{i,j}$ to reproduce the activity of each neuron. To account for the time course of activity we approximated the network equation to be:

$$\tau \frac{d}{dt}\langle f_{i,j}^{k,s}(t)\rangle_j = -\langle f_{i,j}^{k,s}(t)\rangle_j + \Sigma_l w_{i,l}\tanh(\langle f_{l,j}^{k,s}(t)\rangle_j) + \tilde{\kappa}_{GCaMP6s} \times \left(I_i^k(t) + I_i^s(t)\right).$$

We used the approximate kernel $\tilde{\kappa}_{GCaMP6s} = e^{-t/0.7s}$, which reflects the slow decay component of the GCaMP6s response to a burst of spikes (Extended Data Fig. 5). External sensory (I_i^k) and photostimulation (I_i^s) currents were step functions that were active only during the sample and photostimulation epochs, respectively. Fitting was done using a recursive least-square algorithm[30,44] in which all weights on to a given neuron are tuned at each time step to minimize the difference between its modeled and experimentally observed fluorescence activity. Activity from different trial types (k = left and k = right) and photostimulation conditions (s = non., s = pg 1 … pg N) were fit sequentially with nonphotostimulation trials trained first, followed by photostimulation trials. Each fit was iterated 30 times, which produced high-quality fits (median Pearson's correlation = 0.69, range, 0.25–0.92, 75% CI). Repeated fitting produced fits with consistent spatial organization as plotted in Fig. 5j and Extended Data Fig. 8h (data not shown). For each session, two separate fits were obtained, one to capture only nonphotostimulation trials and the other to capture both photostimulation and nonphotostimulation trials.

Statistics. Sample sizes were similar to those used in the field. A statistical power analysis was used to determine the numbers of photostimulation trials required to detect significant behavioral biases. No mice were excluded from analysis. Trial types were presented in a random order during experiments. Experimenters were blind to the animals' behavioral performance on photostimulation versus nonphotostimulation trials during experiments. The 10,000-iteration bootstrapping was performed to determine the significance of behavioral biases on single sessions (Fig. 4a). Pearson's correlation coefficients were used to determine significance in Figs. 2c,d, 3b, 3d, 4b, 4c and 4e.

Reporting Summary. Further information on research design is available in the Nature Research Reporting Summary linked to this article.

Data availability

Two-photon imaging and photostimulation data are available at Figshare (https://doi.org/10.25378/janelia.13546157).

Code availability

Code for network models is available at the Github repository (https://github.com/kpdaie/Daie_targeted_photostim_2020).

References

40. Madisen, L. et al. Transgenic mice for intersectional targeting of neural sensors and effectors with high specificity and performance. *Neuron* **85**, 942–958 (2015).
41. Guo, Z. V. et al. Procedures for behavioral experiments in head-fixed mice. *PLoS ONE* **9**, e88678 (2014).
42. Peron, S. P., Freeman, J., Iyer, V., Guo, C. & Svoboda, K. A cellular resolution map of barrel cortex activity during tactile behavior. *Neuron* **86**, 783–799 (2015).
43. Kwan, A. C. & Dan, Y. Dissection of cortical microcircuits by single-neuron stimulation in vivo. *Curr. Biol.* **22**, 1459–1467 (2012).
44. Sussillo, D. & Abbott, L. F. Generating coherent patterns of activity from chaotic neural networks. *Neuron* **63**, 544–557 (2009).
45. Yang, W. et al. Simultaneous multi-plane imaging of neural circuits. *Neuron* **89**, 269–284 (2016).
46. Packer, A. M. et al. Two-photon optogenetics of dendritic spines and neural circuits. *Nat. Meth.* **9**, 1202–1205 (2012).
47. Yu, Y.-C., Bultje, R. S., Wang, X. & Shi, S.-H. Specific synapses develop preferentially among sister excitatory neurons in the neocortex. *Nature* **458**, 501–504 (2009).
48. Lefort, S., Tomm, C., Floyd Sarria, J.-C. & Petersen, C. C. H. The excitatory neuronal network of the C2 barrel column in mouse primary somatosensory cortex. *Neuron* **61**, 301–316 (2009).

Acknowledgements

We thank R. Darshan, B. Mohar, A. Finkelstein, H. Inagaki, S. Romani, A. Singh, M. Pachitariu and S. Peron for comments on the manuscript; T. Pluntke and R. Mohar for animal training; X. Zhang, K. Ritola and H. Inagaki for making the ST ChrimsonR constructs; E. Fardone for histology; and P. Rickgauer, I. Fiete, B. Kang and T. Wang for discussions. This work was funded by the Howard Hughes Medical Institute. K.D. is a Helen Hay Whitney Foundation postdoctoral fellow and was supported by the Simons Collaboration on the Global Brain.

Author contributions

K.D., K.S. and S.D. conceived and designed the experiments. K.D. performed the experiments and modeling. K.D., K.S. and S.D. analyzed the data and wrote the paper.

Competing interests

The authors declare no competing interests.

Additional information

Extended data is available for this paper at https://doi.org/10.1038/s41593-020-00776-3.

Supplementary information is available for this paper at https://doi.org/10.1038/s41593-020-00776-3.

Correspondence and requests for materials should be addressed to K.S. or S.D.

Peer review information *Nature Neuroscience* thanks the anonymous reviewers for their contribution to the peer review of this work.

Reprints and permissions information is available at www.nature.com/reprints.

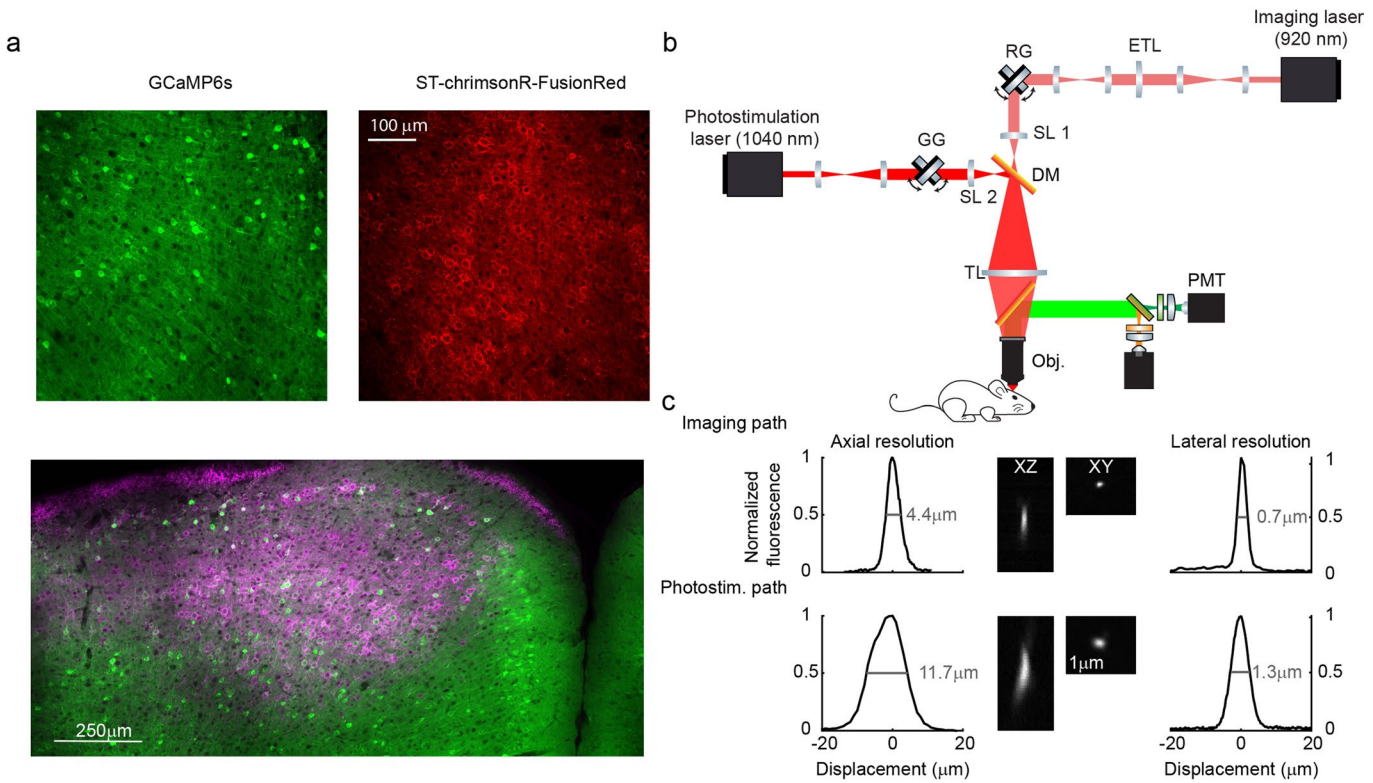

Extended Data Fig. 1 | Coexpression of GCaMP6s and ST-chrimsonR and microscope for simultaneous imaging and targeted photostimulation. After experiments brains were harvested and sectioned (100 μm coronal sections). Images show co-expression of GCaMP6s (green) and ST-chrimsonR-FusionRed (red) from a section that was under the cranial window (n = 1 mouse)**. b**, Schematic of the microscope. Photostimulation laser, 1040 nm (Fidelity HP, Coherent); Imaging laser, 920 nm (Chameleon Ultra II, Coherent); GG, pair of 3 mm galvanometer mirrors (Cambridge, 6215H); ETL, electric tunable lens, (EL-10-30-C, Optotune); SL 2, scan lens photostimulation path, 33 mm focal length, a stack of 3 × 100 mm focal length lenses (AC-254-100b, Thorlabs); SL 1, scan lens imaging path, 30 mm focal length (55-S30-16T, Special Optics); DM, 1000 nm short-pass dichroic mirror (Edmund optics); TL, Tube lens 160 mm focal length (Special Optics); Obj., 16x objective, 0.8 NA, 3 mm working distance (CFI75 LWD, Nikon); PMT, photomultiplier tubes (H10770(P)B-40, Hamamatsu). **c**, Optical point-spread functions. Measurements were made by imaging 500 nm fluorescent beads (YG, Polysciences). Reported values correspond to the full-width at half maximum.

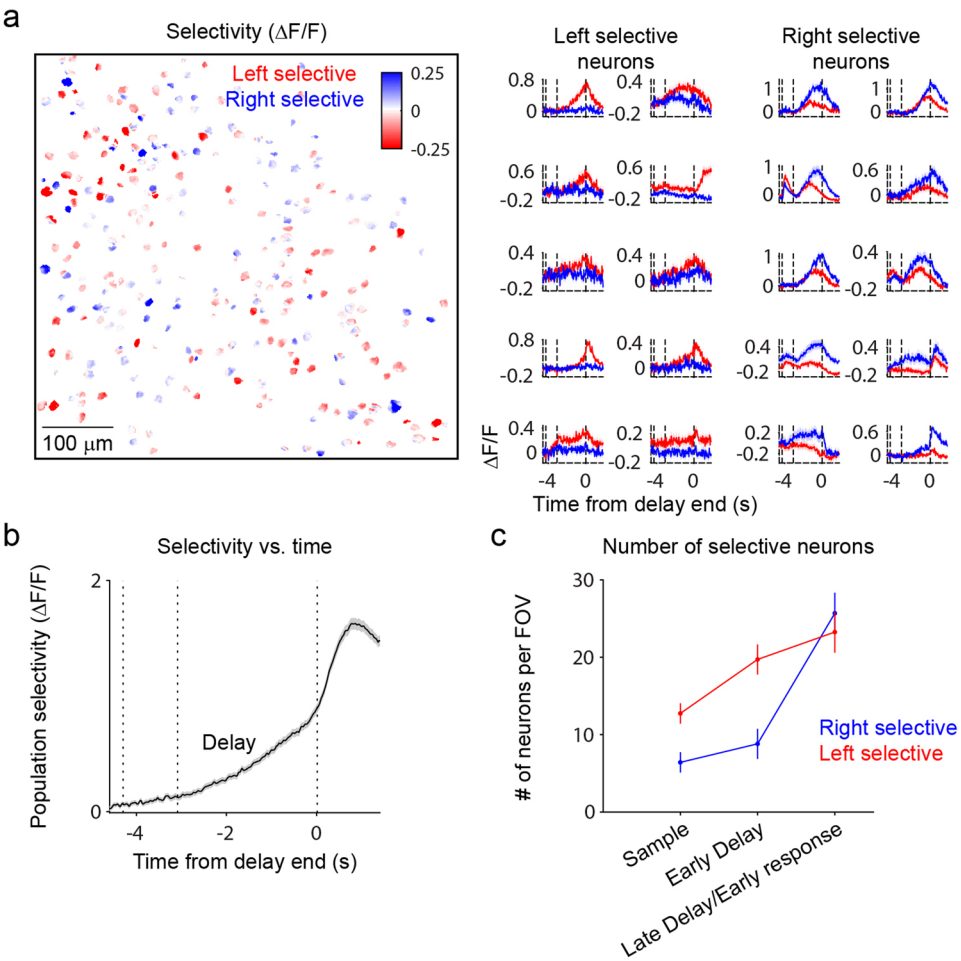

Extended Data Fig. 2 | Trial-type selectivity. a, Left, map of selectivity for individual neurons in one behavioral session. Selectivity was calculated as the difference in activity on correct right and left trials at the end of the delay epoch. Selective neurons were distributed across the field of view. Right, neurons displayed heterogeneous dynamics. Dashed lines, the sample, delay and response epochs. **b**, Selectivity of the neural population based on fluorescence measurements. For each behavioral session all neurons were categorized based on their selectivity at each time point: $V_i^{sel.} = \mathrm{Sign}\left(\langle f_{i,j}^{R,non}(t)\rangle_{j=\text{correct trials train},\, t=epoch} - \langle f_{i,j}^{L,non}(t)\rangle_{j=\text{correct trials train},\, t=epoch}\right)$ where trial averaging was performed over a randomly-chosen training subset of 20% of correct trials denoted as 'correct trials train'. t_{epoch} refers to the 2 s window centered on the end of the delay. The remaining 80% of trials (correct trials test, test subset) were used to compute the population selectivity (PS(t)) as: $PS(t) = 1/\sqrt{\langle N\rangle}\sum_{i=1\ldots N}\left(\langle f_{i,j}^{R,non.}(t)\rangle_{j=\text{correct trials test}} - \langle f_{i,j}^{L,non.}(t)\rangle_{j=\text{correct trials test}}\right)V_i^{sel.}$ where N is the number of neurons in the FOV. Dashed lines, sample, delay and response epochs; (Errorshade s.e.m. across sessions; n = 84 sessions). **c**, Number of selective neurons. A one-tailed T-test was used to compare the epoch-averaged activity on left and right trials for each neuron: $\bar{f}_{i,j}^{R,non.} = \langle f_{i,j}^{R,non.}(t)\rangle_{t=epoch}$ & $\bar{f}_{i,j}^{L,non.} = \langle f_{i,j}^{L,non.}(t)\rangle_{t=epoch}$ Selective neurons are defined as neurons with $p < 0.05$. The epoch labeled 'Late Delay/Early responses' corresponds to the last 0.5 s of the delay and the first 0.5 s of the response, this is the window for which selectivity was calculated throughout the paper. (n = 8 mice, data presented as mean number of neurons with $p < 0.05$; errorbars, s.e.m.).

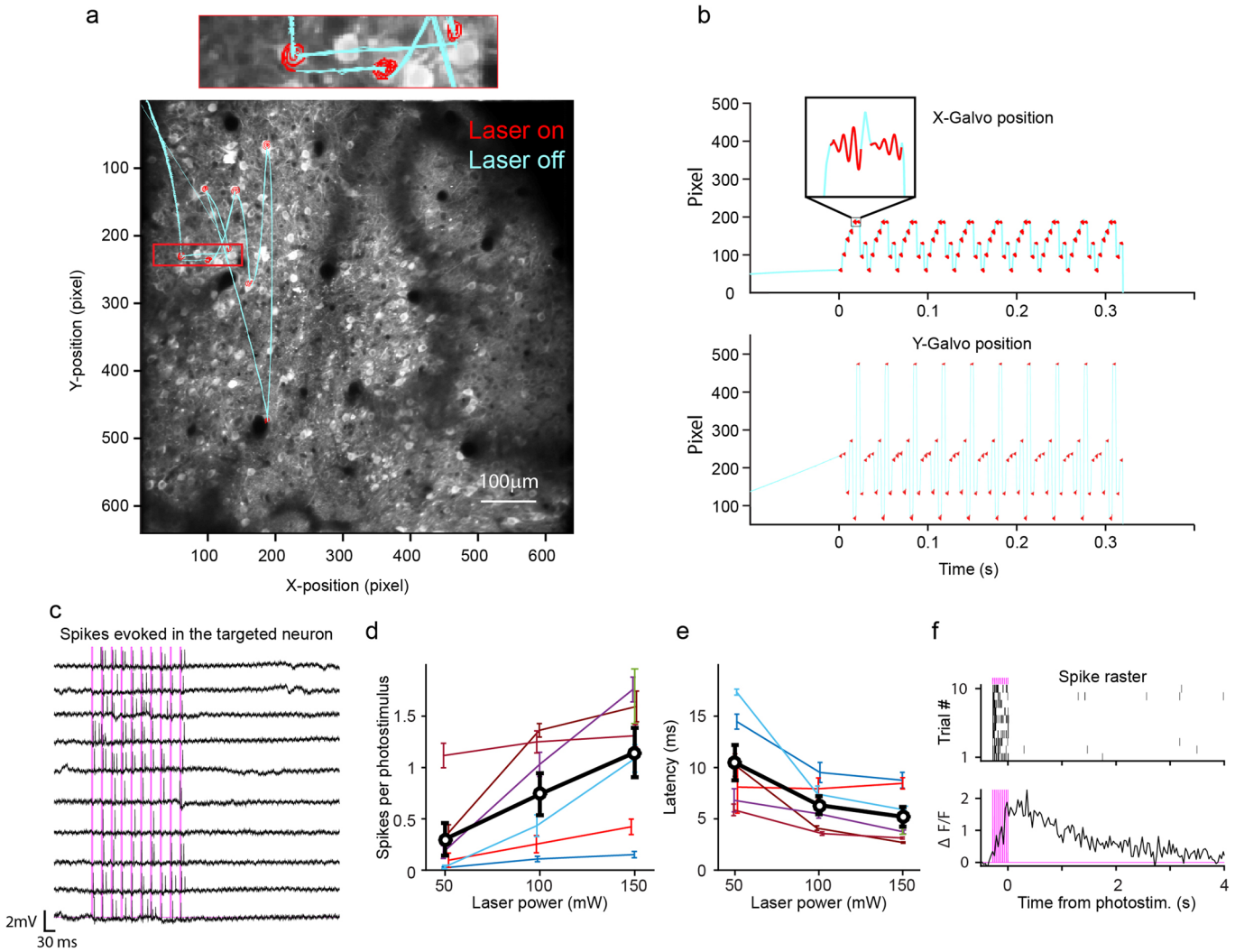

Extended Data Fig. 3 | Electrophysiology during targeted photostimulation. a, Position of photostimulation beam (reconstructed from galvo position encoders). Photostimulation was performed in a spiral pattern (red) that lasted for 3 ms. Laser power was then turned off for 1 ms while the beam was redirected to the next neuron in the sequence (cyan). After the last (8th) neuron was photostimulated the beam was directed back to the first neuron. **b**, Full photostimulation scan trajectory. The sequence across neurons was repeated 10 times per trial and is shown as a trace for the x-position (top) and y-position (bottom). Colors denote laser power state (cyan: off, red: on). (**c-f**), Loose-seal, cell-attached recordings during photostimulation in anesthetized mice. Single neurons (n = 7) were photostimulated using the pattern shown in Extended Data Fig. 3a with laser power of either 50, 100 or 150 mW. **c**. Response of a targeted neuron to photostimulation. Each trace is the response to one train of ten photostimuli (3 ms spirals, 28-ms inter-spiral interval) Magenta bars, photostimuli (150 mW). **d**, Spikes evoked by single photostimuli as a function of laser power. The weakest photostimuli (50 mW) failed to drive spikes in most neurons. All photostimulation experiments done during behavior used either 100 or 150 mW, which evoked on the order of one spike per photostimulus. **e**, Spike latency as a function of laser power. The spike latency for 150 mW was 5 ± 2 ms (b-c, mean ± s.e.m.). Colored lines, data from individual neurons. **f**, Simultaneous GCaMP6s fluorescence and extracellular voltage of one neuron, showing that photostimulation (150 mW) produced increases in spiking that were associated with large increases in fluorescence. Top: spike raster. Each row corresponds to a trial. Spikes marked as vertical lines. Bottom: Trial-averaged fluorescence response. Fluorescence transient decayed with a 1 s time constant, consistent with previous observations[21], and much faster than decay observed when photostimulating groups of neurons during the delay epoch.

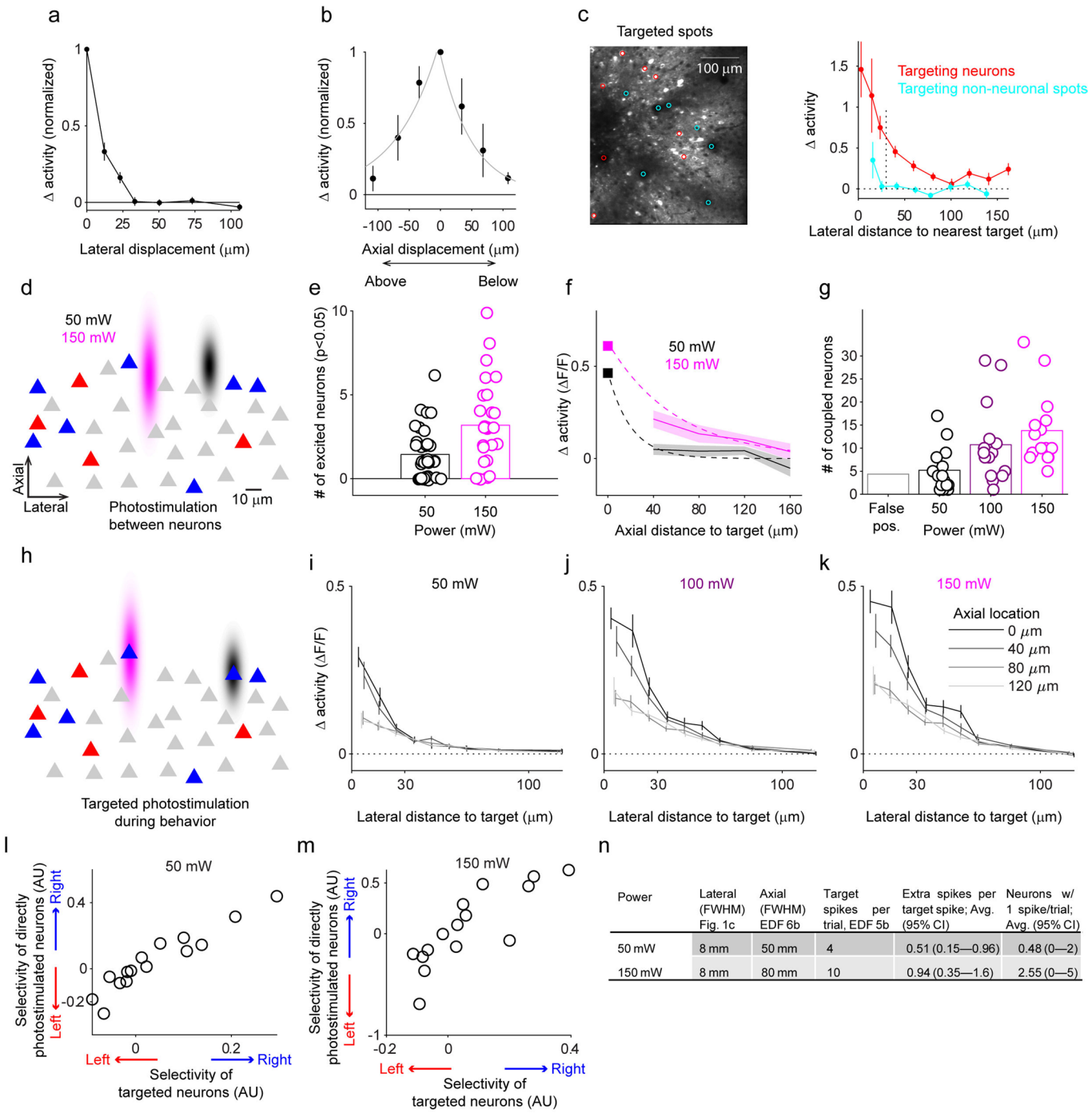

n

Power	Lateral (FWHM) Fig. 1c	Axial (FWHM) EDF 6b	Target spikes per trial, EDF 5b	Extra spikes per target spike; Avg. (95% CI)	Neurons w/ 1 spike/trial; Avg. (95% CI)
50 mW	8 mm	50 mm	4	0.51 (0.15—0.96)	0.48 (0—2)
150 mW	8 mm	80 mm	10	0.94 (0.35—1.6)	2.55 (0—5)

Extended Data Fig. 4 | See next page for caption.

Extended Data Fig. 4 | Spatial resolution of photostimulation. a, Lateral resolution in awake, non-behaving mice. Normalized fluorescence response vs. lateral displacement of the photostimulus with: Δ activity (normalized) = $(f_{post,xy}-f_{pre,xy})/(f_{post,0}-f_{pre,0})$. $f_{pre,xy}$, average fluorescence before photostimulation (150 ms); $f_{post,xy}$, fluorescence averaged immediately after the photostimulation (1 s) with a lateral displacement of xy micrometers from the imaged cell. Changes in activity were limited to a radius of less than 30 micrometers (FWHM, 8 μm). **b**, Axial resolution. $\Delta_{norm.}(z)$ vs. axial displacement of photostimulus (FWHM, 80 μm). (a-b, n = 9 neurons from one mouse, 10 trials for each photostimulus location) **c**, Additional resolution measurements in behaving mice. Left, groups of 8 neurons (red) and 8 non-neuronal spots (cyan) were targeted for photostimulation. Right, photostimulation of the non-neuronal spots produced only weak activation within 20 microns of the photostimulus. We therefore treat neurons located 30 microns or more from a target neuron throughout as 'coupled'. Neurons within 20 μm of a target with altered activity were 'directly photostimulated'. (n = 4 photostim. groups from 2 sessions in 1 mouse; a-c, data presented as mean ± s.e.m.). **d**, Characterization of off-target effects of photostimulation in three dimensions. We imaged 4 planes (n = 3 mice) or 5 planes (n = 1) (350 × 310 μm per plane) separated by 40 μm along the axial dimension. Individual non-neuronal spots were photostimulated in the most superficial plane. **e**, Total number of neurons excited (neurons with $p < 0.05$, one-tailed T-test compared to non-photostim. trials) following photostimulation of individual non-neuronal spots. Neurons located more than 50 μm along the lateral dimension from the targets were excluded from this analysis to restrict detection of excitation to directly photostimulated neurons. Photostimulation of non-neuronal spots with 150 mW excited 3 neurons on average (range 0—9.6, 95% CI, magenta circles, $p < 0.05$, one-tailed T-test). 50 mW photostimuli excited 1 neuron on average (range 0–5, 95% CI, black circles). Given the relatively low density of selective neurons (~20% of the population), these off-target spikes will be mostly in non-selective neurons. (Bar heights, mean number of neurons.) **f**, The amplitude of excitation within 20 μm of the photostimulation beam decays along the axial dimension with $\sigma_{axial} = 30$ μm for 50 mW $\sigma_{axial} = 48$ μm for 150 mW photostimulation (dashed lines) in agreement with ours and previous[45,46] measurements. (Error shade, s.e.m. across targeted spots; b-c, n = 27 spots, 150 mW; n = 38 sites, 50 mW). **g**, The number of coupled neurons in a 350 × 310 μm field-of-view observed during behavior increases with increasing power from 5 (range, 1–9, 75% CI) at 50 mW up to 18 (range, 8–34) for 150 mW. The number of coupled neurons detected during 50 mW photostimulation was not distinguishable ($p = 0.5$, T-test) from the estimated false positive rate of 4 neurons. High power photostimulation therefore improves our ability to probe circuit connectivity. (Bar heights, mean number of neurons.) **h-k**, Spatial spread of photostimulation with 50 mW (**i**), 100 mW (**j**) and 150 mW (**k**) along the axial dimension measured using volumetric imaging during behavior. At 0, 40, 80 and 120 μm below the photostimulation plane excitation decreases with increasing lateral distance from the photostimulus. Excitation is strong in regions directly beneath the photostimulus even when using 50 mW suggesting that much of this out of plane excitation is related to synaptic coupling in a column[47]. Error bars, s.e.m. **l-m**, Selectivity of the targeted neurons vs. selectivity of all directly photostimulated neurons from volumetric imaging experiments. The strong correlation (Pearson correlation, 0.95, 50 mW (c); 0.83 150 mW (d)) indicates that the selectivity of each photostimulation group is dominated by the targeted neurons. **n**, Estimating off-target effects of photostimulation. The photostimulation PSF was modeled as $Ne^{-xy^2/\sigma_{lat.}^2 - z^2/\sigma_{ax.}^2}$, where N is the number of spikes produced by the photostimulus (Extended Data Fig. 3) and the widths σ are calculated based on the FWHM values reported in Extended Data Fig. 4. The number of directly photostimulated neurons and total spikes per photostimulus was estimated using this PSF and the estimated density of cortical pyramidal neurons[48] (10^5/mm^3). Strong photostimuli (150 mW) were estimated to produce an additional 0.94 spikes per spike in the target neuron, distributed across 2–3 non-targeted neurons. Weaker photostimuli (50 mW) have better spatial resolution[46], resulting in a modest reduction in the estimated number of off-target spikes, but also a reduction in the number of target spikes.

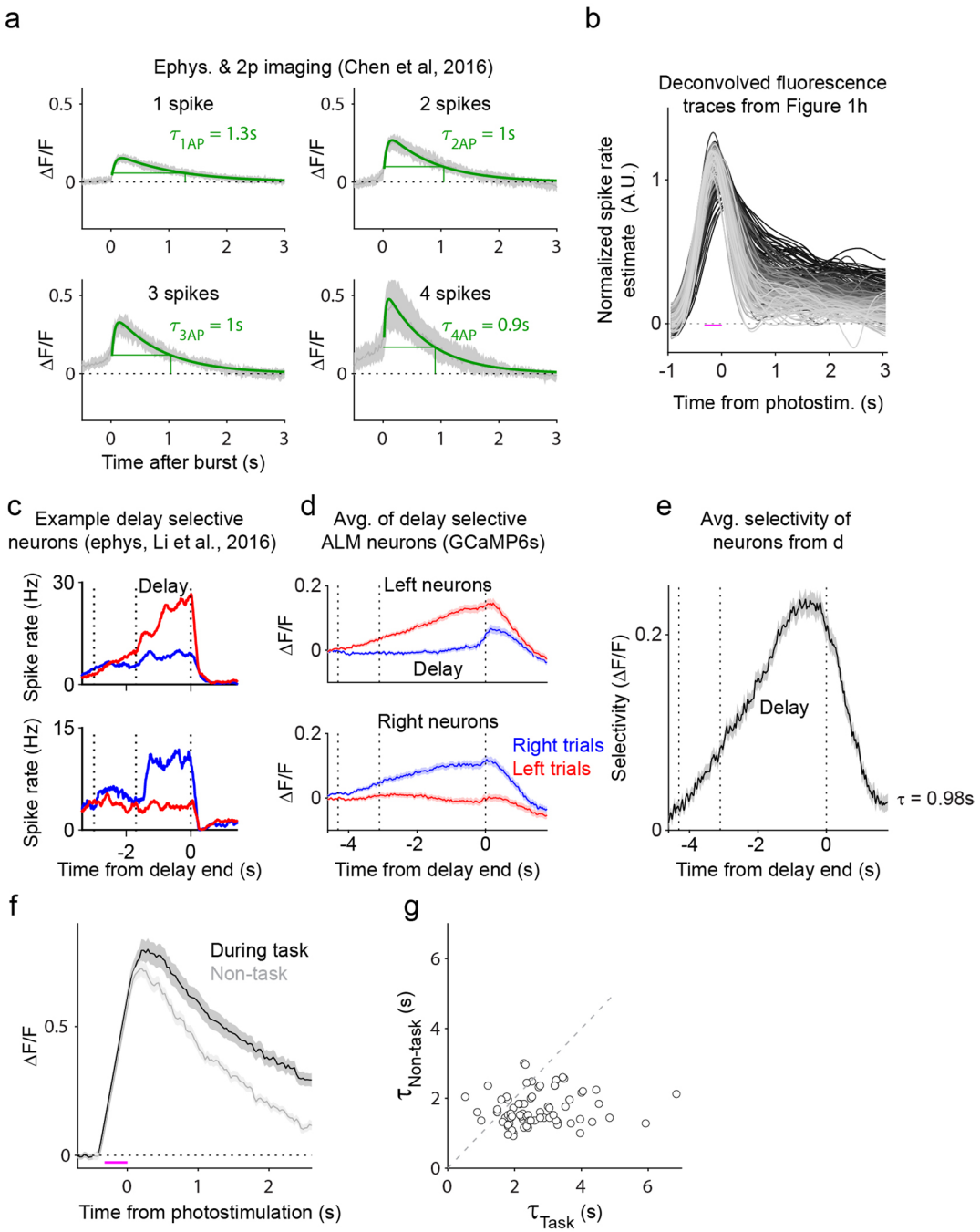

Extended Data Fig. 5 | See next page for caption.

Extended Data Fig. 5 | Dynamics of activity-dependent fluorescence. a, GCaMP6s fluorescence decay after short bursts of spiking activity from visual cortex neurons simultaneously recorded with cell-attached electrophysiology in anaesthetized mice[21,44]. The decay time constant (τ) was defined as the time at which the activity decays to 1/e of its peak value. τ's were 1.2 s, 1 s, 1 s and 0.9 s following bursts of 1, 2, 3 or 4 action potentials respectively. Average fluorescence response kernel was extracted according to the following equation: $\kappa_{GCaMP6s} = Ae^{-t/\tau_{decay}}(1 - e^{-t/\tau_{rise}})$; $A = 0.31$ $\tau_{decay} = 0.87$ s and $\tau_{rise} = 0.06$ s. **b**, Deconvolved fluorescence. Smoothed (MATLAB; csaps, P = 0.96) Δ activity (pg) (Fig. 2b) were deconvolved with $\kappa_{GCaMP6s}$ to estimate the spiking dynamics. 95% of photostimulation groups produce changes in estimated spike rate that remain elevated 2 seconds or longer following photostimulation. **c**, ALM contains neurons in which selectivity peaks at the end of the delay epoch and rapidly decays to zero following the response cue[45]. This rapid decay of firing rate can be used to estimate GCaMP6s τ's during behavior[46]. Extracellular electrophysiological recordings of example neurons with late-delay right (top) and left (bottom) selectivity[45]. **d**, Two-photon imaging of activity in neurons with moderate to strong late delay epoch selectivity (Defined as neurons with $p < 0.2$; two-tailed T-test) and with weak response epoch selectivity (Two-tailed T-test, $p > 0.2$; mean, 13.5 neurons per session, range, 6–22). Top, average response of R neurons. Bottom, average response of L neurons. **e**, Average population selectivity (Extended Data Fig. 2b) of delay selective neurons from d. From the electrophysiological recordings, we assume that spike rate selectivity of these neurons drops to zero. Population selectivity calculated from fluorescence decayed with $\tau = 0.98$ s following the end of the delay, consistent with the measured decay times of GCaMP6s in panel a. This is expected to be an upper bound on the GCaMP6s fluorescence τ because selectivity in some of these neurons may not instantaneously drop to zero and produce erroneously long estimates of τ. **f**, Comparison of persistence during behavioral task vs. non-task periods. The same groups of neurons were photostimulated during behavior and immediately after the animal completed the behavioral session (3 mice, n = 4 sessions, 10 photostimulation groups). Average Δ activity decayed more slowly during the task than in the non-task period. (d-f, Errorshade, s.e.m across photostimulation groups). **g**, Decay time constants for each directly photostimulated neuron (84 neurons) during the task (τ_{task}) and during the non-task period ($\tau_{non\text{-}task}$). τ_{task} (mean, 3.1 s, range, 1.8 s — 4.3 s, 75% CI) were longer than $\tau_{non\text{-}task}$ (mean, 1.7 s, range, 1.2–2.4, 75% CI; $p < 10^{-5}$, two-tailed T-test; errorbars, s.e.m.).

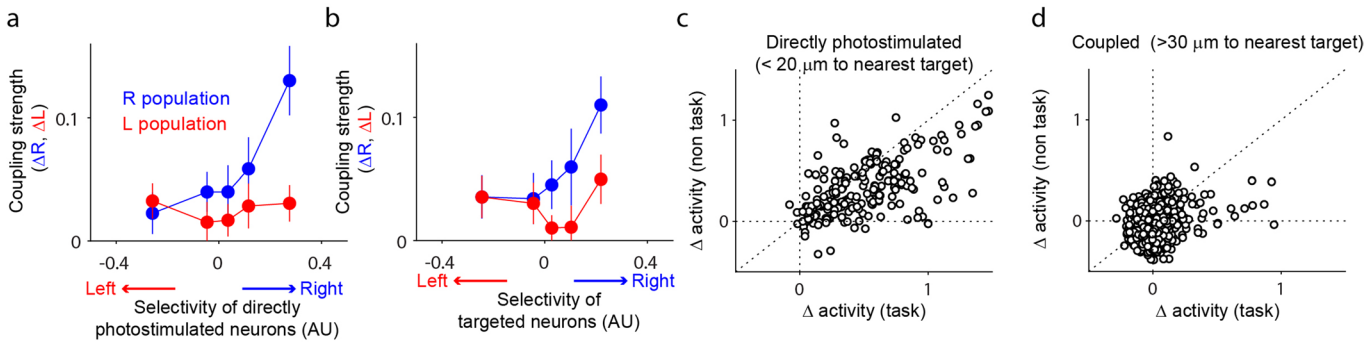

Extended Data Fig. 6 | Functional connectivity. a-b, Relation between coupling strength and selectivity of photostimulation is qualitatively similar whether considering selectivity of targeted neurons or directly activated neurons. **a**, Coupling strength (ΔR and ΔL) vs. average selectivity of directly photostimulated neurons (plot is the same as Fig. 3b). Data were binned in quintiles along x-axis (Error bars, s.e.m.). **b**, Coupling strength vs. average selectivity of targeted neurons. Data were binned in quintiles along x-axis (Error bars, s.e.m., n = 215 photostimulation groups, 8 mice). **c-d**, Coupling strength during behavioral task and non-task period (n = 3 mice, n = 4 sessions, n = 10 photostimulation groups). **c**, Δ activity of directly photostimulated neurons during the non-task period immediately following the conclusion of the behavioral session vs. Δ activity during the task. Response amplitudes were correlated, but the amplitude of excitation is generally much lower ($p < 10^{-5}$, two-tailed T-test) during the non-task period (mean, 0.33, 0.03–0.66, 75% CI) vs. during the task (mean, 0.51, 0.10–0.93, 75% CI). **d**, Δ activity of coupled neurons is also much smaller during the non-task period than during the task ($p < 10^{-5}$, two-tailed T-test).

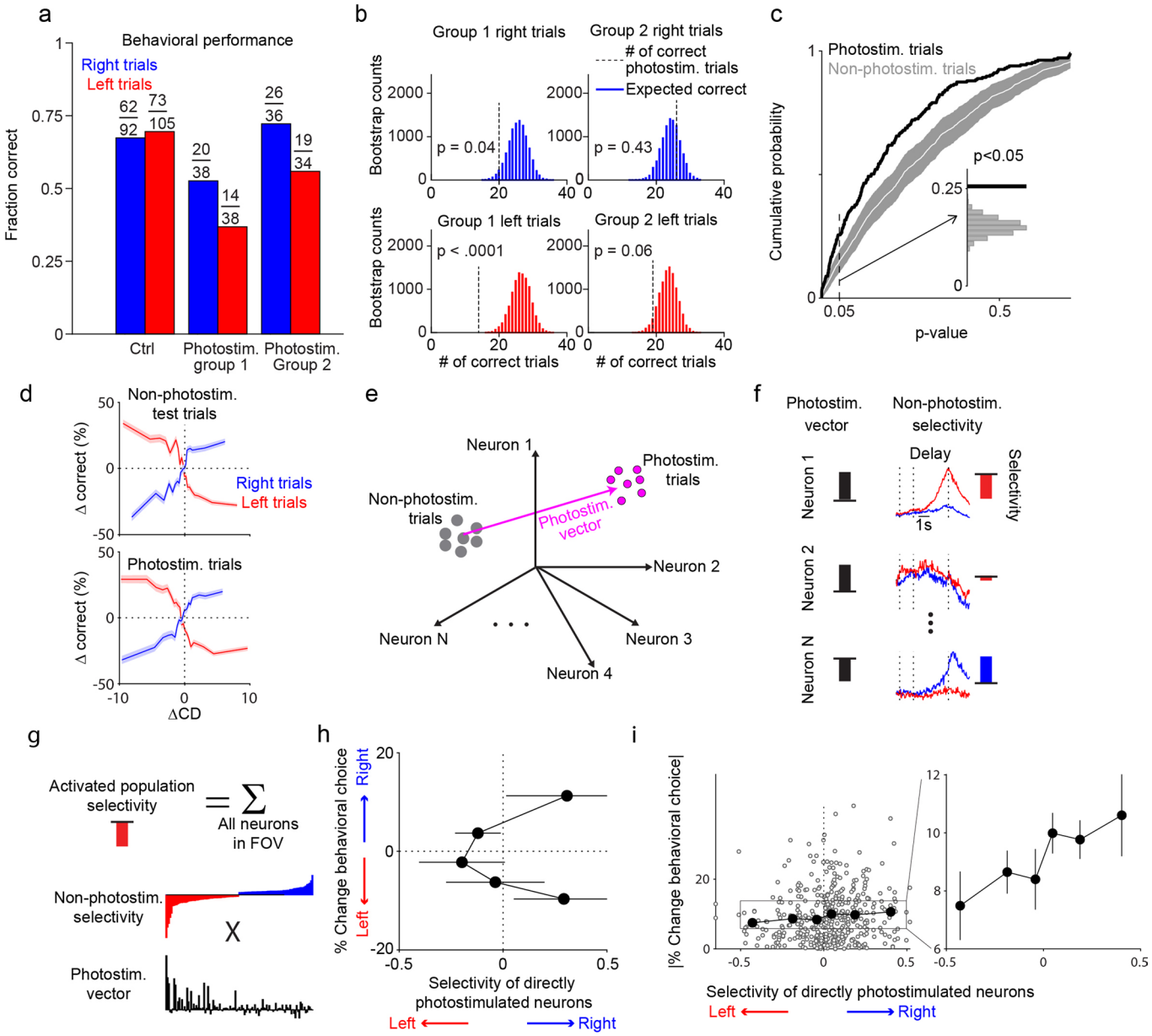

Extended Data Fig. 7 | Effect of photostimulation on behavior. a, Behavioral performance during a single session. Performance dropped from 73/105 correct (69%) on non-photostimulation lick left trials to 14/38 (37%) on photostimulation group 1 trials. **b**, A bootstrap distribution of performance on non-photostimulation trials was generated by randomly sampling 38 of the 105 non-photostimulation trials 10,000 times (b, bottom left). For each of the 10,000 random samplings, we counted the number of correct trials to determine the p-value for each photostimulation group. Bootstrap distributions were used to determine the 95% confidence intervals in Fig. 4a. Changes in performance on left and right trials were uncorrelated for each photostimulation group ($p = 0.27$). This is consistent with the fact that left trials and right trials have very different dynamics, producing different interactions with the same photostimulation **c**, Cumulative distribution of p-values (Two-sided bootstrap (panel b)). from individual sessions (bars from a) for photostimulation (black) and non-photostimulation (white) trials. Gray bar, 95% confidence interval of bootstrap; white line, mean cumulative distribution. Inset: Distribution of photostimulation groups with $p < 0.05$ for photostimulation (black) and non-photostimulation trials (gray). **d**, Δ correct vs. change in activity along a 'coding direction' (CD) which maximally separates trial-averaged activity[14]. CD was calculated using a subset of trials. Single-trial activity from non-photostimulation (top) and photostimulation trials (bottom) was projected along the CD. The relationship between CD activity and behavior was similar for photostimulation and non-photostimulation trials because photostimulation triggered only sparse changes in population activity. **e**, Schematic, photostimulated change in neural population in activity space. To take into account changes caused by photostimulation compared to trial-to-trial changes we computed the photostimulation vector (Methods). **f**, Left, photostimulation vector, contributions of individual neurons. Right, selectivity of individual neurons (S_i, Methods). **g**, Activated population selectivity is the dot product of selectivity (S_i) and the photostimulation vector. **h**, % change in behavioral choice vs. selectivity of directly photostimulated neurons. Data are from an additional 3 mice (separate from the main figures). Large groups (25 neurons) were photostimulated for the full delay epoch (1s) (Error bars, s.e.m.; $n = 27$ photostimulation groups, 3 mice). **i**, Absolute value of % change in behavioral choice vs. selectivity of directly photostimulated neurons (Pearson correlation, 0.1; $p = 0.035$). Dots, average for a single photostimulation group for 1 trial type (right or left trials). Filled circles, mean in equal-spaced bins. Right, magnification of binned data to illustrate trend (Same data as Fig. 4c,d; error bars, s.e.m; $n = 215$ photostimulation groups, 8 mice).

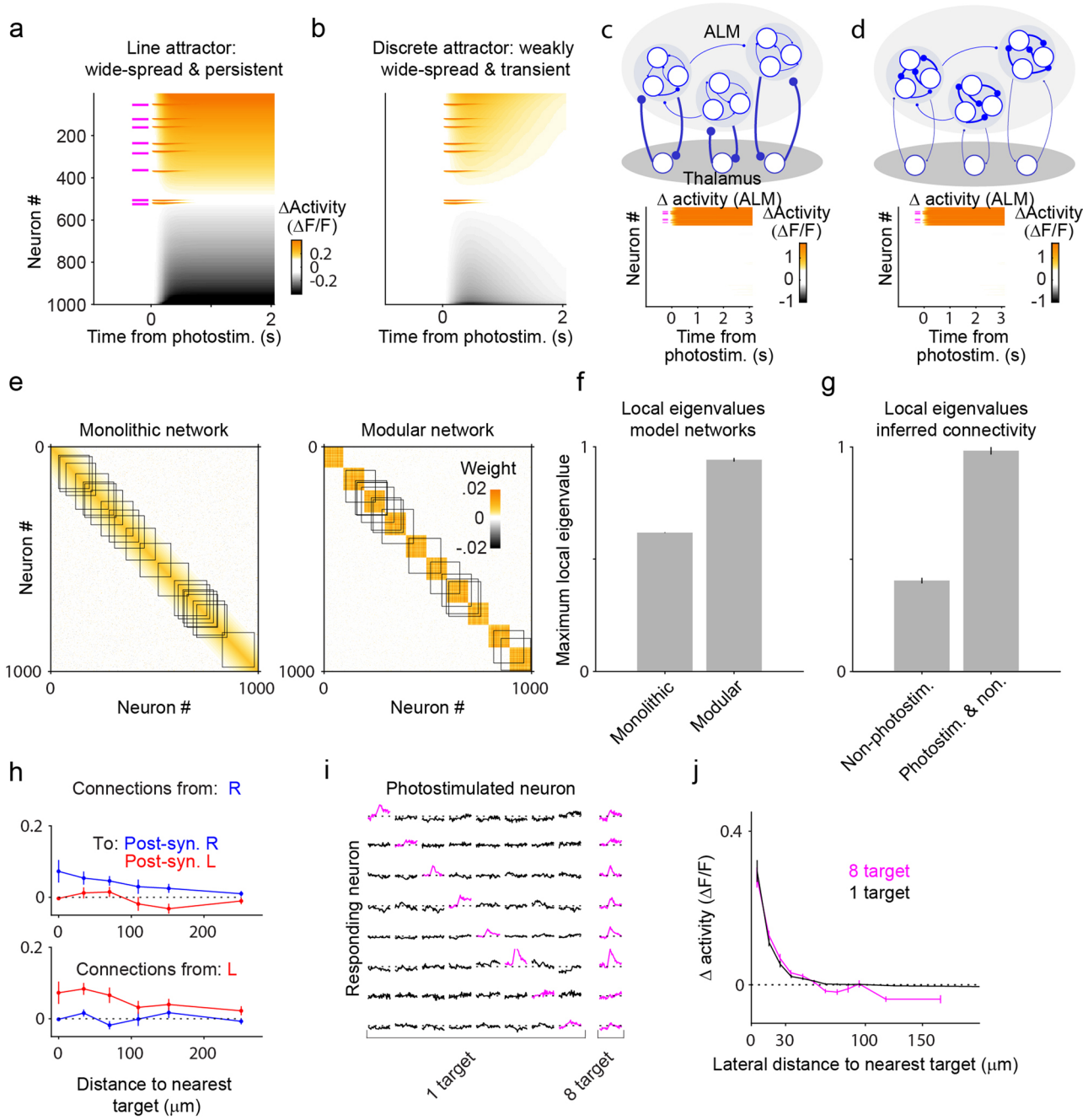

Extended Data Fig. 8 | See next page for caption.

Extended Data Fig. 8 | Models. a-b, Non-modular models fail to recapitulate experimental findings. **a**, Δ activity of a line attractor model to targeted photostimulation of 8 neurons. Photostimulated activity spreads throughout the network. Magenta bars, timing and location of photostimulation. **b**, Δ activity of a discrete attractor model to targeted photostimulation of 8 neurons. This model responds transiently to targeted photostimulation because of the non-linear synaptic connections. See Methods for description of models. **c-d**, Δ activity in models including thalamus and ALM also require modular connectivity. ALM and thalamus are strongly coupled and both contain delay epoch selectivity[33]. **c**, Response of model with modular thalamocortical connections to targeted photostimulation of 8 neurons. **d**. Response of model with modular cortico-cortical connections to targeted photostimulation of 8 neurons. Top, model schematic. Bottom, Δ activity. Model recapitulates the sparse persistent responses to photostimulation. Magenta bars, timing and location of photostimulation. **e-g**, Metrics of modularity from analyzing eigenvalues of subsampled connectivity matrices are consistent with modular structure in networks inferred from the data. The non-modular network in Fig. 4h has a single persistent mode (eigenvalue equal to 1), whereas the modular network has 10 such modes. We develop an analysis aimed at determining which of these two models more closely resembles the connectivity inferred from the data in Fig. 5i,j. **e**, Eigenvalues of subsampled networks. If we were to draw a box around one of the modules in Fig. 5g, we would find that the maximum eigenvalue of this subnetwork is 1, whereas an equivalent box in the non-modular model in Fig. 5h would have a maximum eigenvalue of 0.48. To extend this 'local eigenvalue' analysis to the inferred networks in Fig. 5i,j we wouldn't know which neurons to draw this box around, so to make the analysis more general, we instead draw many boxes at random locations along the diagonal and calculate the maximum eigenvalue of subnetwork within the box. **f**, Modular networks have higher maximum eigenvalue in subsampled networks. Bars indicate the mean of the maximal eigenvalue across 215 subsampled networks for non-modular networks (left) and modular networks (right). On average, the modular network has larger local eigenvalues (mean, 0.94, range, 0.84–1.0, 75% CI) than the non-modular network (mean, 0.62, range, 0.61–63, 75% CI; error bars, s.e.m.). **g**, Maximal eigenvalue in subsampled networks from inferred connectivity implies modular structure. For the inferred connectivity matrix (Fig. 5i,j), we identify all neurons within 70 μm of a photostimulation target whose activity was significantly perturbed by photostimulation (p_i^{pg}<0.05, methods), and calculate the maximum eigenvalue of this subnetwork. Bars indicate the mean of the maximal eigenvalue across 215 subsampled networks for inferred connectivity from non-photostimulated data alone (left) and data with both non-photostimulated trials and photostimulated trials (right). We find that the largest local eigenvalue in networks trained to match photostimulation and non-photostimulation trials was similar to the modular network in Fig. 4g (mean, 0.98, range 0.75–1.27, 75% CI, n = 215 networks). Networks trained to match the activity during non-photostimulation trials only **h**, had a maximum eigenvalue that were similar to the non-modular network (mean, 0.41, range, 0.19–0.62, 75% CI). **h**, Connection weights in networks inferred from non-photostimulated data. Connection weights from presynaptic R (top panel), & L (bottom panel) neurons onto post-synaptic R (blue) and L (red) neurons as a function of distance between neurons. (n = 215 photostimulation groups, 8 mice; Error bars, s.e.m.) **i-j**, Probing spatial scale of modularity with single-target photostimuli. **i**, We photostimulated either 1) a group of eight neurons (8 target) or 2) individual neurons from the group (1 target; n = 4 mice). Traces along diagonal, responses of the targeted neurons (magenta). Neurons within the group were not coupled (off diagonal black traces). **j**, Δ activity vs. lateral distance to nearest target. Excitatory coupling was the same for both 1 target (black) and 8 target (magenta) photostimulation suggesting an absence of cooperativity between neurons in photostimulation groups. 8 target photostimulation produces enhanced inhibition compared with 1 target photostimuli suggesting competitive inhibition between neurons in the photostimulation groups. (Error bars, s.e.m.).

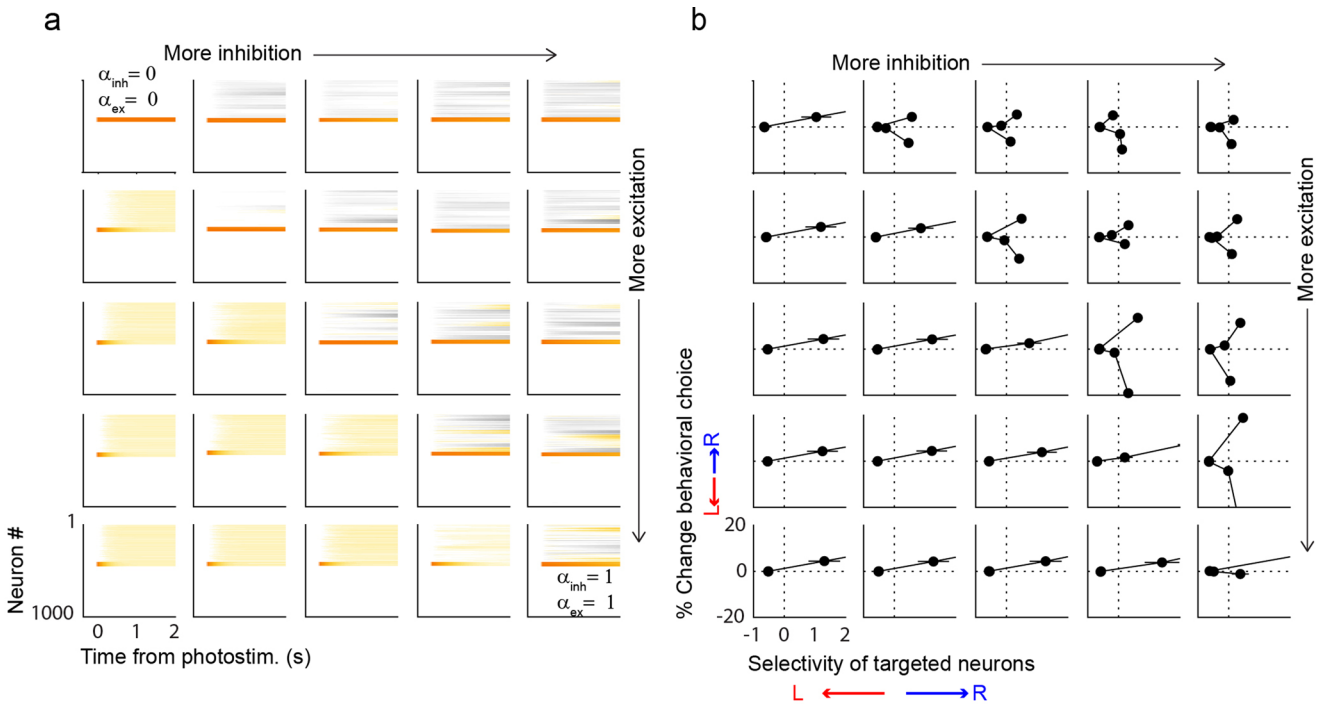

Extended Data Fig. 9 | Network models of responses to both global inhibition and local excitation. Modular network behavior for different strength and sign of inter-modular connections. The modular network shown in Fig. 5g has inter-modular connections with mean $-0.5/M$ and a range from $-1/M$ to 0. Here we vary the mean and amplitude of these inter-modular connections so that inter-module connections have both an excitatory and inhibitory component: $w_{inter} = \alpha_{ex} w_{ex} + \alpha_{inh} w_{inh}$. The scaling factors α determine the respective maximum eigenvalues and were varied from α=0 to α=1. **a**, Heatmap shows difference of activity of all neurons between simulations in which a single module is stimulated and simulations in which no modules were stimulated. Each sub-panel corresponds to a specific values of α_{ex} and α_{inh}. **b**, Change in behavioral output as a function of selectivity of target neurons for each pair of α_{ex} and α_{inh}.

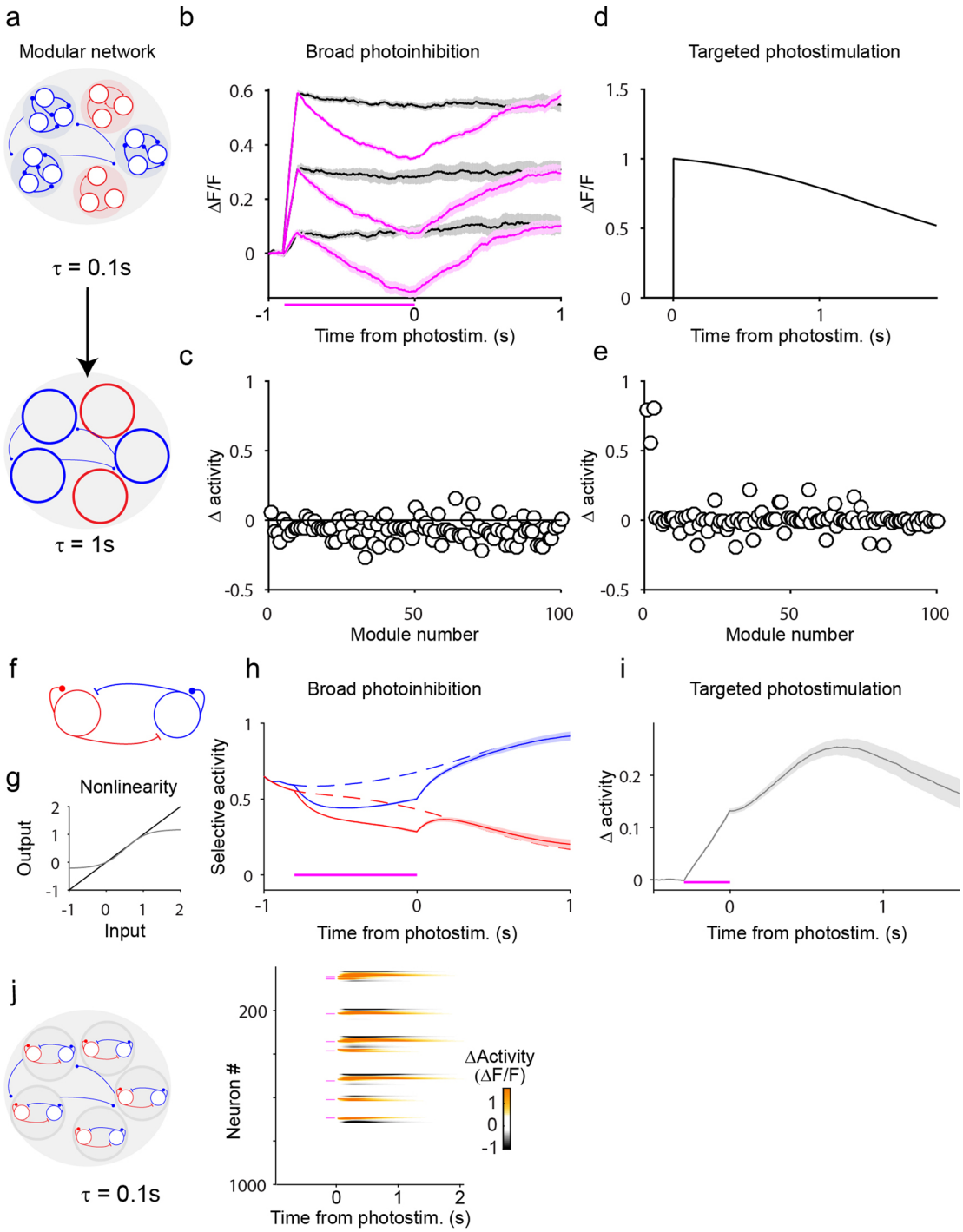

Extended Data Fig. 10 | Modular networks. Two models that match both the current data and previous findings on robustness to global photoinhibition[15]. **a-e**, Robustness through intermodular connections. **a**, Schematic of coarse graining. Magenta traces show the response of the network to broad photoinhibition illustrating the network's robustness to these particular perturbations. Trained networks recovered from photoinhibition and produced graded persistent activity. (Errorshade, s.e.m across repetitions (n = 10)). **c**, Δ activity of each module during photoinhibition. **d-e**, Persistent sparse responses to local excitation. **d**, Average Δ activity of 3 simultaneously photostimulated modules. We note that the persistent response is a consequence of the assumed long intrinsic modular time constants. **e**, Sparse network response (Fig. 2a, Fig. 5f). Δ activity of all modules following photostimulation of modules 1–3. **f-j**, Hybrid discrete/continuous attractor model[14]. **f**, Schematic of the two simulated units. **g**, Shape of the non-linear synaptic function. **h**, Large amplitude inhibition of both neurons produces a rapid recovery. Activity of each of the two simulated neurons is shown for control (dashed line) and perturbation trials (non-dashed). Magenta line shows the duration of inhibition. Perturbation was delivered along the [1,1] direction and thus recovery is fast. Shading indicates s.e.m across 100 simulated trials. **i**, Local excitation produces long transient. Trace, response of one of the units to a brief photostimulation. Magenta line, timing and location of photostimulation. Shading, s.e.m across 100 simulated trials. **j**, Modular hybrid network. Left, schematic of network with ten weakly interacting 100 neuron modules with the synaptic non-linearity shown in g. Right, targeted photostimulation of 8 neurons (magenta lines) produces sparse and persistent activity as in experimental results.

nature research

Corresponding author(s): Karel Svoboda, Shaul Druckmann

Last updated by author(s): YYYY-MM-DD

Reporting Summary

Nature Research wishes to improve the reproducibility of the work that we publish. This form provides structure for consistency and transparency in reporting. For further information on Nature Research policies, see our Editorial Policies and the Editorial Policy Checklist.

Statistics

For all statistical analyses, confirm that the following items are present in the figure legend, table legend, main text, or Methods section.

n/a	Confirmed	
☐	☒	The exact sample size (*n*) for each experimental group/condition, given as a discrete number and unit of measurement
☐	☒	A statement on whether measurements were taken from distinct samples or whether the same sample was measured repeatedly
☐	☒	The statistical test(s) used AND whether they are one- or two-sided *Only common tests should be described solely by name; describe more complex techniques in the Methods section.*
☐	☒	A description of all covariates tested
☐	☒	A description of any assumptions or corrections, such as tests of normality and adjustment for multiple comparisons
☐	☒	A full description of the statistical parameters including central tendency (e.g. means) or other basic estimates (e.g. regression coefficient) AND variation (e.g. standard deviation) or associated estimates of uncertainty (e.g. confidence intervals)
☐	☒	For null hypothesis testing, the test statistic (e.g. *F*, *t*, *r*) with confidence intervals, effect sizes, degrees of freedom and *P* value noted *Give P values as exact values whenever suitable.*
☒	☐	For Bayesian analysis, information on the choice of priors and Markov chain Monte Carlo settings
☒	☐	For hierarchical and complex designs, identification of the appropriate level for tests and full reporting of outcomes
☐	☒	Estimates of effect sizes (e.g. Cohen's *d*, Pearson's *r*), indicating how they were calculated

Our web collection on statistics for biologists contains articles on many of the points above.

Software and code

Policy information about availability of computer code

Data collection	Data collection Scanimage 2016a, Wavesurfer v0.802, Bcontrol, Bpod
Data analysis	Data analysis was done using Matlab 2015a. Code for network models is available at the Github repository (https://github.com/kpdaie/Daie_targeted_photostim_2020)

For manuscripts utilizing custom algorithms or software that are central to the research but not yet described in published literature, software must be made available to editors and reviewers. We strongly encourage code deposition in a community repository (e.g. GitHub). See the Nature Research guidelines for submitting code & software for further information.

Data

Policy information about availability of data

All manuscripts must include a data availability statement. This statement should provide the following information, where applicable:

- Accession codes, unique identifiers, or web links for publicly available datasets
- A list of figures that have associated raw data
- A description of any restrictions on data availability

Two-photon imaging and photostimulation data are available at Figshare.
https://janelia.figshare.com/account/home#/projects/92873

Field-specific reporting

Please select the one below that is the best fit for your research. If you are not sure, read the appropriate sections before making your selection.

☒ Life sciences ☐ Behavioural & social sciences ☐ Ecological, evolutionary & environmental sciences

For a reference copy of the document with all sections, see nature.com/documents/nr-reporting-summary-flat.pdf

Life sciences study design

All studies must disclose on these points even when the disclosure is negative.

Sample size	The numbers of mice, sessions and photostimulation groups were determined by statistical power analysis to maximize our ability to detect alterations in behavioral performance by photostimulation (Methods).
Data exclusions	We did not exclude any animals from data analysis.
Replication	We performed experiments with 8 mice, over 84 experimental sessions to confirm reproducibility.
Randomization	Trial types were presented in a random order.
Blinding	Trials were allocated randomly to photostimulation and non-photostimulation conditions. The effect of photostimulation on coupled neurons and behavior was not monitored during data acquisition therefore researchers not aware of group allocation during experiments.

Reporting for specific materials, systems and methods

We require information from authors about some types of materials, experimental systems and methods used in many studies. Here, indicate whether each material, system or method listed is relevant to your study. If you are not sure if a list item applies to your research, read the appropriate section before selecting a response.

Materials & experimental systems

n/a	Involved in the study
☒	☐ Antibodies
☒	☐ Eukaryotic cell lines
☒	☐ Palaeontology and archaeology
☐	☒ Animals and other organisms
☒	☐ Human research participants
☒	☐ Clinical data
☒	☐ Dual use research of concern

Methods

n/a	Involved in the study
☒	☐ ChIP-seq
☒	☐ Flow cytometry
☒	☐ MRI-based neuroimaging

Animals and other organisms

Policy information about studies involving animals; ARRIVE guidelines recommended for reporting animal research

Laboratory animals	15 mice; Emx1-Cre X CamK2a-tTA X Ai94(TITL-GCaMP6s) & slc17a7 IRES Cre 1D12 X CamK2a-tTA X Ai94(TITL-GCaMP6s); both males and females; Ages P70-P150.
Wild animals	The study did not involve the use of wild animals.
Field-collected samples	The study did not involve field-collected samples.
Ethics oversight	All procedures were in accordance with protocols approved by the Janelia Institutional Animal Care and Use Committee.

Note that full information on the approval of the study protocol must also be provided in the manuscript.